PAPER

# Reduced model for direct induction startup scenario development on MAST-U and NSTX-U

To cite this article: D.J. Battaglia *et al* 2019 *Nucl. Fusion* **59** 126016

IOP Publishing | International Atomic Energy Agency Nuclear Fusion

Nucl. Fusion **59** (2019) 126016 (22pp) https://doi.org/10.1088/1741-4326/ab3bd5

# Reduced model for direct induction startup scenario development on MAST-U and NSTX-U

**D.J. Battaglia[1], A.J. Thornton[2], S.P. Gerhardt[1], A. Kirk[2], L. Kogan[2] and J.E. Menard[1]**

[1] Princeton Plasma Physics Laboratory, Princeton, NJ, United States of America
[2] United Kingdom Atomic Energy Authority, Culham Centre for Fusion Energy, Culham Science Centre, Abingdon, Oxon OX14 3DB, United Kingdom of Great Britain and Northern Ireland

E-mail: dbattagl@pppl.gov

Received 10 May 2019, revised 12 August 2019
Accepted for publication 16 August 2019
Published 3 October 2019

**Abstract**

A reduced semi-empirical model using time-dependent axisymmetric vacuum field calculations is used to develop the prefill and feed-forward coil current targets required for reliable direct induction (DI) startup on the new MA-class spherical tokamaks, MAST-U and NSTX-U. The calculations are constrained by operational limits unique to each device, such as the geometry of the conductive elements and active coils, power supply specifications and coil heating and stress limits. The calculations are also constrained by semi-empirical models for sufficient breakdown, current drive, equilibrium and stability of the plasma developed from a shared database. A large database of DI startup on NSTX and NSTX-U is leveraged to quantify the requirements for achieving a reliable breakdown ($I_p$ ~ 20 kA). It is observed that without pre-ionization, STs access the large $E/P$ regime at modest loop voltage ($V_{loop}$) where the electrons in the weakly ionized plasma are continually accelerating along the open field lines. This ensures a rapid (order millisecond) breakdown of the neutral gas, even without pre-ionization or high-quality field nulls. The timescale of the initial increase in $I_p$ on NSTX is reproduced in the reduced model provided a mechanism for impeding the applied electric field is included. Most discharges that fail in the startup phase are due to an inconsistency in the evolution of the plasma current ($I_p$) and equilibrium field or loss of vertical stability during the burn-through phase. The requirements for the self-consistent evolution of the fields in the weakly and fully-ionized plasma states are derived from demonstrated DI startup on NSTX, NSTX-U and MAST. The predictive calculations completed for MAST-U and NSTX-U illustrate that the maximum $I_p$ ramp rate ($dI_p/dt$) in the early startup phase is limited by the voltage limits on the poloidal field coils on MAST-U and passive vertical stability on NSTX-U.

Keywords: spherical tokamak, inductive startup, NSTX, MAST

(Some figures may appear in colour only in the online journal)

## 1. Introduction

Direct induction (DI) startup on a tokamak device generates loop voltage using a central solenoid coil in order to ionize (i.e. breakdown) a neutral gas and induce a toroidal plasma current ($I_p$) [1]. Breakdown is facilitated by producing open helical field lines with long connection lengths via a region of low poloidal magnetic field ($B_\theta$) and large toroidal magnetic field ($B_T$) in the vacuum vessel (i.e. a magnetic field null). Following breakdown, the magnetic and electric fields must evolve self-consistently in order to increase $I_p$ and maintain the radial and vertical position of the plasma.

The recent complementary upgrades of the two largest spherical tokamak (ST) experiments (NSTX to NSTX-U

 

[2], and MAST to MAST-U [3]), require development of DI scenarios for the new devices. Similar to most tokamaks, DI startup is accomplished on these devices by feed-forward (i.e. pre-programming) control of the solenoid and poloidal field coil currents. The startup period encompasses the pre-charging of the coil currents and pre-filling the vacuum vessel to a target neutral pressure, the breakdown of the neutral gas and the initial ramp-up of $I_p$ where the electron temperature increases (i.e. burn-through). The startup period ends when $I_p$ is large enough that the solenoid and PF currents are controlled via active feedback on the measured $I_p$ and inferred plasma boundary. This is typically when $I_p$ exceeds the total induced current in conducting structures ($I_p > I_{wall} \sim 200$ kA on NSTX and MAST). Changes to the passive conducting structures, coils and power supplies on NSTX-U and MAST-U compared to NSTX and MAST, respectively, motivate the redevelopment of the feed-forward current targets in the startup phase.

Beyond achieving a reliable startup scenario, the scientific mission of these STs benefits from the optimization of the DI startup scenario. Long-pulse (5–10 s) operation on the upgrade devices relies on minimizing the volt-second consumption of the startup scenario [4]. In addition, startup scenarios aim to maximize the plasma current ($I_p$) ramp rate ($dI_p/dt$) and boundary elongation in order to facilitate a broad current distribution (low internal inductance or low-$l_i$) and minimize pressure peaking [5]. A large $I_p$ ramp rate shortens the time between breakdown and achieving a suitable neutral beam heating efficiency in order to induce the L–H transition and 'lock in' a broad current profile by slowing the current diffusion rate [6]. Hardware capabilities and plasma instabilities can limit $I_p$ ramp rate and boundary elongation in the startup phase.

High-fidelity calculations have recently demonstrated good quantitative agreement with the breakdown [7] and burn-through [8] processes on tokamaks that elucidate the physical processes of DI startup. DI scenario development efforts benefit from faster reduced models for the plasma initiation that encompass both the breakdown and burn-through processes in order to efficiently develop and test time-dependent coil current, neutral fueling and pre-ionization parameters [9].

This paper summarizes a reduced model employed to optimize the feed-forward coil currents and gas prefill pressure for reliable DI startup on NSTX-U and MAST-U. The reduced model is a fast (less than one minute) calculation that uses a unified framework for both ST experiments. This work extends the DI scenario development completed for the first operations on NSTX-U that enabled DI startup at different levels of solenoid precharge and $V_{loop}$ [10].

Figure 1 describes the framework of the model. The rectangles with a thick border and italic text describe the free parameters of the model while the four gray boxes highlight comparisons or metrics evaluated in predictive calculations. Given the time-evolving feed-forward solenoid, poloidal field (PF) and toroidal field (TF) currents, the time-dependent vacuum field evolution is computed using the LRDFIT code[3] that includes currents induced in conductive structures. The

[3] https://nstx-u.pppl.gov/software/lrdfit

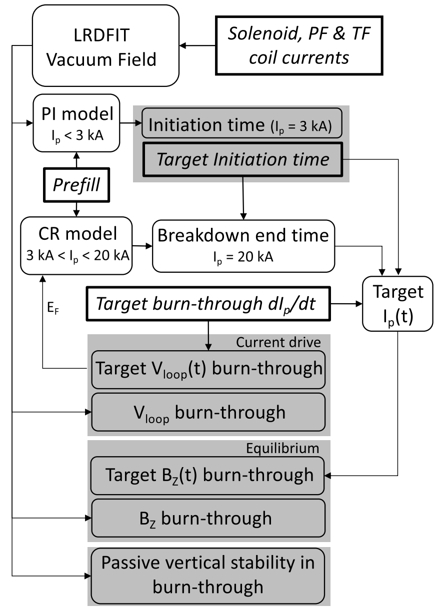


**Figure 1.** Schematic of reduced model used to develop DI scenarios.

LRDFIT code is described in section 2 and the four ST experiments considered in this paper (NSTX, NSTX-U, MAST and MAST-U) are described in section 3 with a focus on the characteristics that influence the vacuum field evolution and the DI startup scenario.

A new aspect of this work is the development of a fast, semi-empirical breakdown model that computes the timing of the plasma initiation and the length of time required to produce a plasma density that exceeds the neutral density with an $I_p$ of approximately 20 kA. The breakdown model is divided into two phases, PI (pre-ionization) and CR (current rise). The PI model is used to determine the timing of the initial plasma formation ($I_p \sim 3$ kA) given the evolution of the vacuum fields and the vessel prefill. In predictive calculations, the timing of the plasma initiation ($I_p = 3$kA) is compared to the target initiation time. The CR model is used to provide a conservative timescale for the plasma to transition from partially ionized to fully ionized with $I_p = 20$ kA. The timescale is computed using an average electric field that combines the minimum $E$ field required for initiating the discharge and sustaining the discharge in burn-through ($E_F$ in figure 1). The details of the PI and CR models are described in section 4 and compared to discharges from NSTX and NSTX-U. The breakdown model incorporates elements of recent high-fidelity [7] and reduced models [11] to achieve good agreement with the observed breakdown phenomenology. The development of a reduced model framework tested against a large database of startup discharges supports ongoing efforts to develop and test reduced models for DI startup that can be applied to future tokamaks such as ITER [12, 13].

Following breakdown, $I_p$ in the fully-ionized discharge increases from about 20 to 200 kA and the applied fields must evolve self-consistently. Section 5 describes the development of semi-empirical metrics for evaluating the ohmic current-drive, equilibrium and stability of the plasma given the time-dependent vacuum field calculations and a target $I_p$ evolution. The new aspect of this work is the development of metrics specific to low-aspect-ratio ST plasmas where the current is primarily located in a vertical sheet near the inboard limiter.

Section 6 illustrates the utility of the reduced DI startup model to complete predictive calculations for NSTX-U and MAST-U where the feed-forward solenoid and PF coil currents are tailored to satisfy operational limits and achieve $I_p > 150$ kA within 20 ms of the start of the solenoid current ramp. The predictive calculations illustrate that the maximum $I_p$ ramp rate ($dI_p/dt$) in the startup phase is limited by the voltage limits on the poloidal field coils on MAST-U and passive vertical stability on NSTX-U. A summary of this work is presented in section 7.

## 2. Time-dependent vacuum field calculations using LRDFIT

The vacuum field calculations described in this paper use the LR Circuit Model with Data Fitting (LRDFIT) code written in the IDL programming language [14, 15]. The LRDFIT code was developed to compute the free-boundary Grad–Shafranov equilibrium including the induced currents in the axisymmetric conducting structures. The approach of this solver (similar to EFIT++ [16] used on MAST) is to first compute the induced currents in discrete toroidally conductive elements using coupled circuit equations where the plasma is treated as resistive conducting elements and SVD regularization of the plasma current density distribution is used to produce an over-constrained system of equations. The self- and mutual-inductance of the toroidally conductive elements is computed by dividing the elements into rectangles [14] with cross-sectional area of 0.25–1.0 $cm^2$ and grouped into discrete elements where the passive elements (conductive structures excluding magnetic field coils) are associated with a unique voltage loop measurement [17]. The work in this paper does not compute the plasma equilibrium, it only uses the 'front-end' of the LRDFIT code to solve the coupled circuit equations to compute the induced currents with $I_p = 0$ (i.e. vacuum fields).

The front-end of the LRDFIT code is routinely used at NSTX for calibrating magnetic measurements, refining the axisymmetric wall model [17] and developing DI scenarios [10]. LRDFIT has recently been expanded to perform similar calculations for MAST and MAST-U. The location of toroidally conductive structures, poloidal field coils and magnetic measurements is derived from machine drawings. The resistance of the conductive structures is estimated using the properties of the bulk material. The series and parallel connections between coils, and in some cases, passive conductive elements are also included when defining the circuit equations.

Dedicated vacuum shots are used to calibrate the magnetic measurements, modify the resistance, location and grouping of the passive elements and refine the position and orientation of magnetic sensors. This is typically an iterative process that uses a combination of error minimization and intuition about the device construction to continually refine the machine description. NSTX and MAST operated for many years enabling a mature machine description. Agreement between the measured and modelled magnetic measurements for vacuum shots was typically within 1% during periods with slowly changing magnetic fields and within 5% in periods with rapidly changing fields typical of startup scenarios. NSTX-U completed one experimental campaign in 2016 before terminating operations to fix a failed divertor coil and make changes to the machine design; the refinement of the machine description did not attain the maturity of the NSTX model. Restarting operations on NSTX-U will require further refinement of the DI scenario realized in 2016 due to changes in the conducting structures and the desire to further optimize the scenario beyond what was demonstrated. At the time of this publication, the MAST-U facility is preparing for its first experimental campaign, including the first vacuum shots toward refining the machine description derived solely from machine drawings.

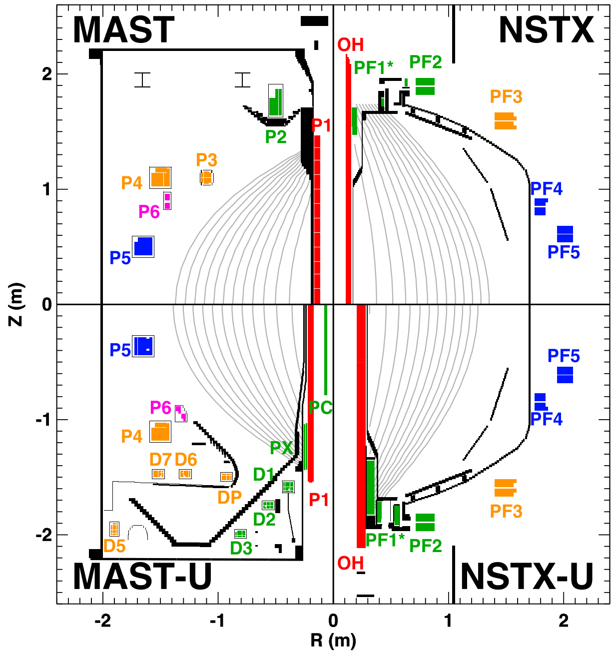


**Figure 2.** Poloidal cross section of the four ST devices described in this paper. Each quadrant of the image is a different device. Black lines show the toroidally conductive structures while the colored regions show the active coils as described in the text. Gray contours are flux surfaces of the ohmic solenoid (OH or P1) fringing field.

## 3. Direct induction capabilities and constraints

### 3.1. Magnetic field coils

Figure 2 shows one half of a poloidal cross section for each of the four ST devices considered in this paper. The black elements are the toroidally conductive axisymmetric structures while the colored regions are the active coils that will be described throughout this section. The coils on NSTX and

NSTX-U reside outside the vacuum boundary whereas all coils except P1 and PC reside inside the vacuum boundary on MAST and MAST-U. All elements are nearly up-down symmetric with the exception of the PF1 coil sets on NSTX (only the upper configuration of the PF1 coil sets is shown).

The toroidal magnetic field ($B_T$) is clockwise ($-\phi$) and $I_p$ is counter-clockwise for all four devices. The central solenoid (red coils) is precharged to a positive current ($+\phi$), producing a field in the confining $B_Z$ ($-Z$) direction inside the vacuum vessel with poloidal curvature that is good for vertical stability. The light gray contours in figure 2 show illustrative flux surfaces of the solenoid field excluding any contribution from induced currents in the conductive structures. The field has larger poloidal curvature on MAST(-U) compared to NSTX(-U) due to the shorter length of the central solenoid.

Nulling of the solenoid fringe field is primarily accomplished using positive current ($+\phi$) in large-R coils that are off midplane (orange coils). The nulling field is produced on NSTX and NSTX-U using the PF3 coil set and on MAST and MAST-U using one or more D-coils. DI startup was employed only in dedicated experiments on MAST [18] (merging-compression startup was primarily used for most operations) and the DI scenarios produced the nulling field using the P3 or P2 coil sets.

One important consideration for the maximum ramp rate of $I_p$ is the voltage available to change the current in the PF coils to vary the equilibrium vertical magnetic field ($B_Z$). On NSTX and NSTX-U, the PF3 upper and lower coils are each driven with a 2 kV power supply for a maximum total voltage of 4 kV. On MAST, a high voltage capacitor bank power supply could provide up to 4 kV on the P3 coils. On MAST and MAST-U, the P4 set is wired in series with a single 560 V power supply. MAST-U will not employ a capacitor bank power supply and must supplement P4 and P5 with a number of D-coil sets powered by 700 V H-bridge circuits in order to produce a flux swing, and thus $I_p$ ramp rate, similar to MAST, NSTX and NSTX-U.

Low-R coils (green coils) with $+\phi$ current reduce the radial curvature of the solenoid field near the inboard midplane. However, these fields reduce the passive vertical stability, especially if the plasma boundary grows vertically as the plasma current increases. NSTX and NSTX-U do not employ low-R coils in the startup scenario; however, MAST-U will most likely employ these coils in the DI breakdown scenario in order to generate a sufficiently large field null with a shorter solenoid compared to NSTX-U. The PC coil (inboard midplane) on MAST-U is not employed in the startup scenarios due to the desire to minimize the heating and stress on this coil.

All four devices have similar near-midplane large-R coil sets (blue coils) with the up-down pair wired in series and driven by a single, unipolar power supply driving $-\phi$ current to produce confining field. These coil sets produce a vertical field with curvature that destabilizes the vertical stability and reduces the vertical extent of the field null. Therefore, these coils typically do not carry current until after breakdown and are not operated near the voltage maximum; the current ramp rate in the large-R coils is limited by the desire to maintain good field curvature.

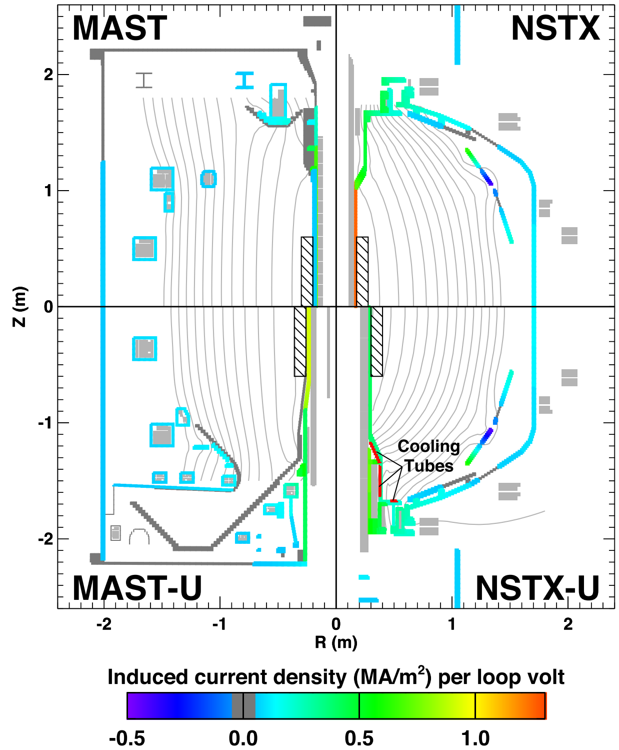


**Figure 3.** Current density induced in the toroidally conductive structures by ramping the solenoid current to produce an average of one loop volt in the black hashed rectangle for each device. Gray contours are flux surfaces due to the induced current.

Since both the low-R off-midplane divertor coils (positive current ramping to zero) and large-R near midplane coils (zero current ramping negative) tend to reduce vertical stability, there is a trade-off to using these coil sets in the startup scenario. Generally, it is preferable to minimize the use of the positive current in the low-R coils such that a larger ramp rate of the large-R coil current can be used for a given constraint on the poloidal field curvature. This reduces the voltage demand on the other PF coils for a given target $I_p$ ramp rate. This must be balanced by the desire to use the low-R coils to increase the vertical extent of the field null.

### *3.2. Induced currents*

The currents induced in the passive structure are important to include in startup calculations, particularly in the case of the rapid $I_p$ ramp rate favored by ST experiments to facilitate broad current profiles. Figure 3 shows the current density in conductive components induced by the change in the solenoid current that produces an average of $V_{loop} = +1$ V in the hashed region of figure 3 using the LRDFIT code. A majority of the induced current is positive ($+\phi$), thus in the same direction as $I_p$. The lone exception occurs in regions of the passive plates on NSTX and NSTX-U where the magnitude of the eddy currents on the surface of the highly-conductive toroidally-segmented plates is greater than the toroidal current loop through the resistive connections between the plates.

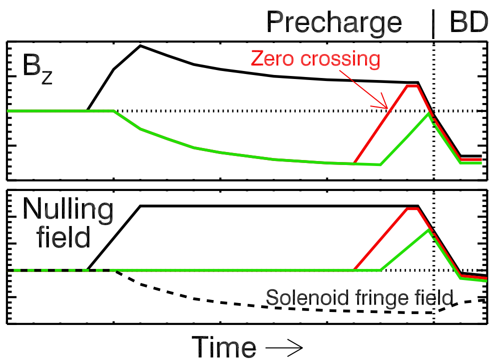


**Figure 4.** Cartoon of different precharge strategies. The top panel shows $B_Z$ in the breakdown region, bottom panel shows the $B_Z$ contributions from the solenoid and nulling coils. The implications for the prefill timing and scenario reproducibility for each strategy are described in the text.

The light gray contours in figure 3 indicate the flux surfaces of the field produced by the induced current. The induced field on MAST and MAST-U does not have a big impact on the passive vertical stability since the flux surfaces are mostly vertical near the midplane. However, NSTX and NSTX-U have a larger radial field component resulting in flux surfaces with more poloidal curvature. With positive $V_{\text{loop}}$, the field from the induced currents is in the deconfining direction, thus the radial field component decreases the passive vertical stability.

The reduction in the passive vertical stability from induced currents was an issue in the first operational campaign of NSTX-U in 2016 due to an error in construction. A series of cooling tubes behind the divertor tiles (labeled in figure 3) were constructed using copper instead of Inconel. This error was realized during the first vacuum shots on NSTX-U when the induced current in the polar regions (top and bottom of the centre column) was significantly larger than expected. The vacuum field calculations indicate that the current density in the low resistance cooling tubes was between 15–30 MA m$^{-2}$ for $V_{\text{loop}} = 1$ V (note that this is well above the extreme of the color bar). Post mortem analysis of the cooling tubes indicated that heating from the induced currents melted and severed the cooling tubes, leading to complex paths for the induced current that most likely changed throughout the first campaign. NSTX-U is presently undergoing a rebuild of the polar regions and a number of design changes will reduce the induced current, including the installation of Inconel cooling tubes. The impact of the larger induced current in the polar regions on the NSTX-U startup scenario will be discussed in sections 5 and 6.

### *3.3. Pre-charge and pre-ionization*

The precharge evolution must be included in the vacuum field calculations since the induced currents will influence the startup phase. Figure 4 is a cartoon summarizing three different precharge strategies where the central solenoid current is increasing from zero to the maximum current over a period of time (typically 0.5–2 s). NSTX and NSTX-U use a precharge scenario represented by the black lines where the nulling field provided by the PF coils is imposed for the duration of the solenoid precharge in order to prevent a null ($B_Z \sim 0$) prior to the breakdown (BD) phase. This approach does not restrict the timing of the prefill and permits active feedback on the vessel pressure using ion gauge pressure measurements with slow (~10 ms) time response. Active feedback of the prefill pressure improves the reliability of the breakdown scenario since the gas load required to meet the target prefill depends on the wall conditions and the status of the neutral beam gate valves and pumps.

Conversely, MAST-U aims to minimize the heating of the D-coils in the precharge phase, and thus will use a scenario represented by the red lines in figure 4. This strategy requires delaying the start of prefill gas fueling until after the zero crossing and using feed-forward control of the fueling rate. The calculations presented in this paper in section 6 assume the gas fueling begins 15 ms prior to the targeted breakdown time, similar to MAST. The final scenario shown in figure 4 (green lines) further reduces the magnitude and duration of the nulling field coils by approaching the null condition from $-B_Z$ as opposed to $+B_Z$. This scenario does not restrict the timing of the prefill but is not favored because small changes in the field strengths can result in significant changes to the evolution of the startup, reducing the reproducibility of the scenario.

Pre-ionization (PI) systems can reduce the $V_{\text{loop}}$ required for initiating the plasma and expand the operational range of viable startup regimes. NSTX and NSTX-U have a dedicated electron cyclotron heating (ECH) system that injects up to 30 kW of power at 18 GHz [19]. Emissive filaments mounted to the outboard wall are used concurrently, however the magnetic field structure is not tailored to direct the emitted electrons into the breakdown region. MAST employed a variety of PI systems in dedicated DI experiments including emissive filaments, an ultraviolet flash lamp, a 7 J ruby laser pulse (from the Thomson scattering system) and the neutral beam [18]. Similarly, MAST-U will use emissive filaments and may use the Thomson laser and/or NBI system as additional PI sources.

The next sections will quantify the utility of PI on NSTX and NSTX-U and demonstrate that reliable scenarios without PI are expected to be feasible. This is an important result since MAST-U will have reduced PI capabilities compared to MAST and the utility of the ECH PI system on NSTX-U is expected to diminish as the resonance layer of the fixed frequency ECH system moves to larger $R$ at higher $B_T$.

## 4. Reduced breakdown model

DI startup is typically described as progressing through three plasma phases: breakdown, burn-through and ramp-up. The breakdown phase includes the avalanche ionization process where the plasma transitions from a weakly-ionized plasma to a fully-ionized plasma. The end of the breakdown phase is typically defined as the time of the largest $D_\alpha$ emission since it roughly corresponds to the equalization between the decreasing neutral density and the increasing plasma density. The burn-through phase features a rise in the electron temperature (from

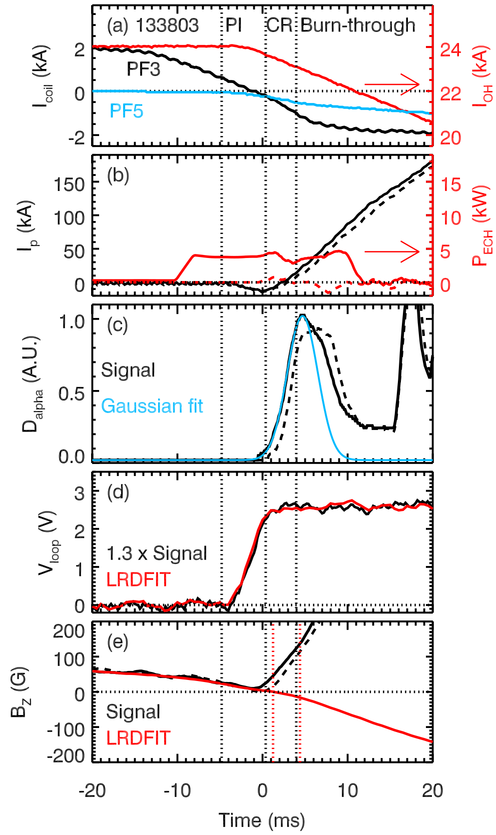


**Figure 5.** Typical DI startup scenario on NSTX. (*a*) Current in the solenoid (red), PF3 (black) and PF5 (blue) coils. (*b*) Measured plasma current (black) and ECH PI power (red). Two discharges are shown, with (solid) and without (dashed) ECH PI. (*c*) Radial midplane $D_\alpha$ signal (black) and a Gaussian fit of the initial rise (blue). (*d*) Scaled $V_{loop}$ measured at the inboard midplane (black) compared to the $V_{loop}$ at 0.22 m computed using LRDFIT (red). (*e*) $B_Z$ measured near the inboard midplane (black) compared to the $B_Z$ at 0.22 m using LRDFIT (red). Vertical dotted lines separate the precharge, pre-ionization (PI), current rise (CR) and burn-through phases.

the order of 10 to 100 eV) progressing through the ionization (i.e. burn-through) of impurity ion charge states with considerable energy lost to radiation [8]. In the ramp-up phase, the energy confinement and flux consumption achieve a level consistent with typical L-mode operation on tokamaks.

### *4.1. DI startup on NSTX*

Figure 5 shows a typical DI scenario on NSTX with a prefill of 42 $\mu$Torr (discharge 133803). The current in the ohmic solenoid (red) and the PF3 (black) and PF5 (blue) is shown in figure 5(*a*). The toroidal field coil current (not shown) is constant through the startup phase and produces $B_T = 1.8$ T at $R = 0.22$ m. The plasma current ($I_p$) measured by a Rogowskii coil is shown in figure 5(*b*) (solid black). The dip in $I_p$ below zero is due to an imperfect correction for the induced vessel currents within the Rogowskii loop. The ECH PI power injected is also shown in figure 5(*b*) (solid red) with a maximum power around 4 kW. The dashed black and red lines are for a discharge with an identical prefill and coil currents but did not have ECH PI (133765). As shown with these two discharges, ECH PI has a small impact on the evolution of breakdown on NSTX when operating with a prefill greater than 20 $\mu$Torr and with low impurity content.

Figure 5(*c*) shows a $D_\alpha$ signal from a filterscope with a radial view along the midplane for both discharges (black and dashed black). The initial rise of the $D_\alpha$ signal has a gaussian form as shown by the light blue line. The abrupt rise in the $D_\alpha$ signal after $t = 15$ ms is due to neutral gas injection from outboard gas injectors. The loop voltage evolution of both discharges is very similar since the feed-forward evolution of the solenoid and PF currents are nearly identical. The red line in figure 5(*d*) is the $V_{loop}$ at $R = 0.22$ m on the midplane from a vacuum field LRDFIT calculation. The loop voltage measured by a flux loop at the inboard midplane at $R = 0.16$ m (solid black) provides a good estimate for the calculated $V_{loop}$ at $R = 0.22$ m (solid red) when multiplied by a factor of 1.3.

Figure 5(*e*) compares the $B_Z$ at $R = 0.22$ m from the vacuum field calculation (red) to the $B_Z$ measured slightly below the midplane and at a smaller $R$ (black). This measurement is made by integrating the voltage from a Mirnov coil and correcting for toroidal field pickup, which results in an uncertainty in the signal offset on the order of 20 Gauss (0.1% of $B_T$) on NSTX. The $B_Z$ measurement is the most sensitive diagnostic to the start of the discharge that is routinely available within the NSTX dataset, as seen by the rapid increase in $B_Z$ toward positive values near $t = -1$ ms. For typical breakdown conditions, the plasma density is inferred to be on the order of $10^{16}$–$10^{17}$ m$^{-3}$ (about 1%–10% of the neutral density) in order to produce a measurable difference from the vacuum field on the Mirnov coil (order 15 Gauss corresponding to about 3 kA of plasma current).

The vertical black lines in figure 5 designate critical times in the breakdown phase. The earliest vertical line is the point when the loop voltage ($V_{loop}$) exceeds 0.1 V and is used to define the start of the breakdown phase. The central vertical line indicates the 'initiation time' and corresponds to the rapid rise in $B_Z$ for the solid black case (discharge with ECH PI). It is identified as an increase in 15 Gauss above the minimum in the measured $B_Z$ signal during the breakdown phase. The rightmost black line marks the end of breakdown phase and is defined as time required to increase an additional 100 Gauss on the $B_Z$ measurement after the Initiation time for the solid black case. The two time periods within the breakdown phase are labelled 'PI' (for pre-ionization) and 'CR' (for current rise). The vertical red dotted lines in figure 5(*e*) indicate the different starting and ending times of the CR phase for the discharge without ECH PI (black dashed traces).

In the PI phase, the loop voltage is increasing while $B_Z$ is positive and decreasing due to the decrease in the PF3 coil current. The sign convention follows the description in section 2 where positive $B_Z$ is the deconfining direction. At the end of the PI phase (i.e. the initiation time), the plasma density is on the order of $10^{17}$ m$^{-3}$, while the neutral density remains ~$10^{18}$ m$^{-3}$. The plasma density increases an additional order of magnitude until it is comparable to the neutral density over the next 4 ms during the CR phase. The $V_{loop}$ is driven primarily by the solenoid and the vacuum $B_Z$ field (red line in figure 5(*e*)) changes sign to the confining direction. The field generated by the plasma current quickly overwhelms the vacuum magnetic field on the inboard side of the breakdown region, facilitating the formation of closed magnetic surfaces. The plasma resistivity during the CR phase is differentiated from the burn-through phase because the electron temperature is unable to rise above 10 eV due to considerable thermal ionization of the neutral gas. At the end of the CR phase, the plasma density is expected to be on the order of $10^{18}$ m$^{-3}$ for typical prefill values.

The analysis of DI startup on NSTX and NSTX-U in the remainder of this section identifies the transition between the three phases (PI, CR and burn-through) using the measurement of the $B_Z$ at the inboard midplane as shown in figure 5. Specifically, the increase in $B_Z$ above the minimum value is 15 G at the transition between the PI and CR phases and 115 G at the transition between the CR and burn-through phases. The 15 G threshold at the initiation time (between PI and CR phases) was found to be large enough to exclude most time periods where pre-ionization was able to sustain a sufficient plasma density such that a finite plasma current ($I_p$ ~ 1 kA) was sustained for typical loop voltages, yet $I_p$ was not rapidly increasing (i.e. no ionization avalanche). The 115 G threshold used to define the end of the breakdown phase is a proxy for the timing of the $D_\alpha$ peak since the $B_Z$ measurement is available for more discharges in the NSTX and NSTX-U database compared to the $D_\alpha$ signal. The relationship between the rise in the $B_Z$ signal and the $D_\alpha$ peak was developed using a database of about 10 000 discharges where the $D_\alpha$ peak could be reliably identified.

The reduced model presented in this paper recasts the thresholds between each phase of startup (PI, CR and burn-through) in terms of the plasma current (figure 1) derived using an assumed current density located close to the inboard limiter on NSTX, NSTX-U and MAST-U. The results of the predictive calculations are not overly sensitive to the chosen thresholds in $I_p$ and $B_Z$ provided the semi-empirical model is derived from data using consistent definitions. The equivalent $I_p$ threshold for devices of different scales requires a similar evaluation of typical conditions in the breakdown phase, particularly for the definition of $I_p$ corresponding to the peak of the $D_\alpha$ signal.

*4.1.1. Reduced model for the PI phase.* The reduced model presented in this section computes the evolution of the plasma density and $I_p$ during the pre-ionization phase using a time-evolving axisymmetric vacuum field structure and a neutral prefill pressure. The 2D region-of-interest (ROI) used to estimate the plasma position for computing the source and loss rate of the plasma is optimized at each time step to maximize the increase in $I_p$.

The plasma current in the PI phase is assumed to be entirely due to the parallel drift motion of the electrons:

$$I_p = \frac{eN_e v_{De}}{2\pi R_C}\cos\theta \quad (1)$$

where $N_e$ is the number of electrons, $v_{De}$ is the average parallel electron drift velocity, $R_C$ is the major radius of the current centroid and $\theta$ is the field line pitch angle such that $\sin\theta$ ~ $B_\theta/B_T$. The rate of increase in the number of charge carriers during the avalanche process is [20]

$$dN_e/dt = N_e\, v_{De}\,(\alpha - 1/L) \quad (2)$$

where $L$ is the effective connection length of the helical field lines. The neutral ionization rate ($\alpha$) is given by

$$\alpha[\mathrm{m}^{-1}] = AP\exp(-BP/E) \quad (3)$$

where $P$ is the prefill and $E$ is the parallel electric field ($E_\parallel = E_T\cos\theta$) and the Townsend coefficients for deuterium are $A = 510$ m$^{-1}$ Torr$^{-1}$ and $B = 1.25\times10^4$ V m$^{-1}$ Torr$^{-1}$. The form of equation (2) implies that the plasma density ($n_e$) rises exponentially over a time period $t_{br}$

$$n_{ef}/n_{e0} = \exp(t_{br}\, v_{De}(\alpha - 1/L)) \quad (4)$$

where $n_{e0}$ is the starting electron density and $n_{ef}$ is the final electron density and it is assumed the plasma volume, electron drift velocity, electric field and effective connection length are constant over the time period.

In the regime $E/P < 20$ kV m$^{-1}$ Torr$^{-1}$, the electrons are assumed to achieve a constant $v_{De}$ due to collisions with neutral molecules:

$$v_{De} = \eta_{br}\left[\frac{\mathrm{m^2\,Torr}}{\mathrm{V\,s}}\right]\frac{E}{P} \quad (5)$$

where $\eta_{br}$ is 43 for deuterium [20] giving $v_{De} < 10^6$ m s$^{-1}$. In the regime $E/P > 20$ kV m$^{-1}$ Torr$^{-1}$, the electrons are predicted to be constantly accelerating instead of achieving a constant drift velocity [20]. This 'runaway' regime is due to the fact that the cross-section of the electron and neutral molecule collision has a maximum around 4 eV ($v_{De}$ ~ $10^6$ m s$^{-1}$). The average loss time of the electrons accelerating along the open field lines is

$$t_{loss} = \left(\frac{2Lm}{eE}\right)^{1/2} \quad (6)$$

where $e$ and $m$ are the electron charge and mass, respectively. Thus, the average velocity of the electrons during the acceleration is approximated to be

$$v_{De} = \left(\frac{eEL}{2m}\right)^{1/2}. \quad (7)$$

The predicted free acceleration of the electrons results in an order-of-magnitude increase in the average electron drift velocity and a comparable reduction in the breakdown timescale compared to the regime with constant drift velocity (equation (5)). STs readily access the large $E/P$ regime at modest $V_{loop}$ since $E$ ~ $E_T = V_{loop}/2\pi R$.

Good agreement between the initial increase in $I_p$ observed on NSTX and the reduced model requires a mechanism for reducing the applied $E_\parallel$ consistent with a number of experimental and computational studies that find the rise in the density evolves slower than what is expected from the exponential form of equation (4). Recent work using particle-in-cell calculations have proposed that charge separation can reduce the parallel electric field influencing the electron drift velocity once the electric field generated over a Debye length becomes sufficiently large at high density [7, 21, 22]. The charge separation induced by electron motion along open helical field lines produces a self-generated $E$ field that opposes the applied $E$ field and scales as [7]:

$$E_{\rm self} \sim \sqrt{\frac{n_{\rm e} kT_{\rm e}}{\epsilon_0}}\, \gamma \sin\theta \qquad (8)$$

where $\gamma$ is a parameter describing the geometry of the charge separation that has a value between zero and one and becomes smaller as the loss points of the open field lines become farther apart for a given plasma volume. The calculations in this paper use $\gamma = 0.08$ which is consistent with highly elongated plasma boundaries; using an approximation developed for a uniform vertical field with a fixed rectangular plasma boundary ($\gamma = (2/\pi)\tan^{-1}(W/H)$ where $W$ and $H$ are the width and height of the rectangle, respectively) derived in [7] produces a similar result in the reduced model. The calculations also assume that $E_{\rm self}$ can only be as large as 75% of the applied $E_{\|}$ field. This ad hoc maximum ratio is consistent with the results reported in [7]. The self-generated parallel electric field reduces the parallel drift velocity of the electrons and the timescale of the avalanche process. Additionally, the perpendicular field induces $E \times B$ drifts that reduce the connection length in regions of low field line pitch (i.e. a field null).

One critical aspect of developing a reduced model based on time-dependent axisymmetric vacuum field calculations is defining a 2D ROI that approximates the plasma boundary when averaging the vacuum magnetic and electric fields. The reduced model assumes the ROI is a rectangle centered on the midplane and has the inner boundary at the inboard limiter radius (see hashed region in figure 3, for example). The width and height of the ROI are chosen at each time point of the vacuum field calculations to maximize the increase in the plasma current normalized by the plasma density, derived using equations (1)–(3):

$$\frac{1}{en_{\rm e}}\frac{{\rm d}I_{\rm p}}{{\rm d}t} = S_{\rm ROI}\, v_{\rm De}^2 \left(AP\exp\left(-B\frac{P}{E_{\rm avg}}\right) - \frac{1}{L_{\rm avg}}\right)\cos\theta_{\rm avg} \qquad (9)$$

where $S_{\rm ROI}$ is the cross-section surface area of the ROI, and $E_{\rm avg}$, $L_{\rm avg}$ and $\theta_{\rm avg}$ are the average parallel electric field, effective connection length and field line pitch angle within the ROI, respectively. The electron parallel drift velocity ($v_{\rm De}$) is determined from equations (5) and (7) (using $E_{\rm avg}$ and $L_{\rm avg}$) where the runaway definition (equation (7)) is used when $E_{\rm avg}/P > 20\,{\rm kV\ m^{-1}\ Torr^{-1}}$.

Data presented later in this section suggest the maximum effective connection length ($L$) achieved on NSTX and NSTX-U is on the order of 400 m. This inferred connection length is about a factor of five smaller than the average connection length computed using field line following [23] or using basic assumptions for the field structure. A number of processes can shorten the loss time beyond what is expected from parallel electron transport along helical field lines, including non-axisymmetric fields, particle drifts [7], and diffusion [24]. Thus, the calculation of $L_{\rm avg}$ requires a reasonable approximation for these effects. An approach similar to calculations performed by Ejiri *et al* (equations (5), (6) and (8) in [11]) defines the effective connection length within a rectangular ROI ($L_{\rm avg}$) as:

$$L_{\rm CZ} = \frac{1}{2}\frac{H_{\rm ROI}}{\langle |B_{\rm Z}|\,/\,|B_{\rm T}|\rangle} = \frac{\mu_0 I_{\rm TFrod}}{4\pi}\frac{H_{\rm ROI}}{\langle R\,|B_{\rm Z}|\rangle} \qquad (10a)$$

$$L_{\rm CR} = \frac{1}{2}\frac{W_{\rm ROI}}{\langle |B_{\rm R}|\,/\,|B_{\rm T}|\rangle} = \frac{\mu_0 I_{\rm TFrod}}{4\pi}\frac{W_{\rm ROI}}{\langle R\,|B_{\rm R}|\rangle} \qquad (10b)$$

$$L_{\rm avg} = \left[L_{\rm CZ}^{-2} + L_{\rm CR}^{-2}\right]^{-1/2} \qquad (10c)$$

where $H_{\rm ROI}$ and $W_{\rm ROI}$ is the full height and full width of the ROI, respectively, and the brackets indicate the average value over the 2D ROI. Equations (10*a*)–(10*c*) consider the average vertical ($Z$) and radial (R) components of the field line pitch related to the size of the ROI. The average inverse field ratios impose that the areas with the largest pitch angle inside the ROI have the largest impact on the average loss rate (~1/$L$). The factor of ½ in equations (10*a*)and (10*b*) reflects that, on average, electrons are born in the center of the ROI. The choice of the ROI aspect ratio ($H_{\rm ROI}/W_{\rm ROI}$) where $L_{\rm CZ} = L_{\rm CR}$ corresponds to the largest achievable $L_{\rm avg}$ for a fixed surface area.

Equation (9) is maximized at each timepoint in the calculation by solving over a range of $H_{\rm ROI}$ and $W_{\rm ROI}$ and identifying the maximum in the 2D solution space. The width and height are allowed to be as small as 5 cm and the maximum size is defined by the limiter boundaries. The results presented in this paper vary the width and height dimensions by 1 cm to produce the 2D solution space; this resolution is sufficient to capture the spatial variation in the fields. The results are most sensitive to the choice of the time resolution required to resolve the exponential increase in the density. The results in this paper interpolate the time-dependent vacuum field calculations to a 1 $\mu$s time resolution since this was found to provide a sufficient optimization of computing efficiency and insensitivity to a factor-of-two variation in the time resolution.

*4.1.2. Comparison of PI model with selected discharges.* Figure 6 demonstrates the breakdown model described by equations (1)–(10) derived from the time-dependent vacuum field calculations for the DI scenario shown in figure 5 and demonstrates good agreement with the timing of the initial rise in $I_{\rm p}$. Figure 6(*a*) shows the density evolution for three separate calculations. The black traces represent a case with pre-ionization where the initial density of the plasma is large ($8 \times 10^{16}\ {\rm m^{-3}}$), while the red and light blue traces start at a low plasma density ($n_{\rm e} = 10\ {\rm m^{-3}}$). The red case allows the electron velocity to increase an order of magnitude in the runaway regime (equation (7)), while the light blue case assumes a constant drift velocity for all times (equation (5)). The dotted horizontal line in figure 6(*a*) indicates the plasma density equal to 15% of the initial atomic (i.e. twice the molecular) neutral density and is an approximate threshold for electron–ion collisions to become more frequent than electron–neutral

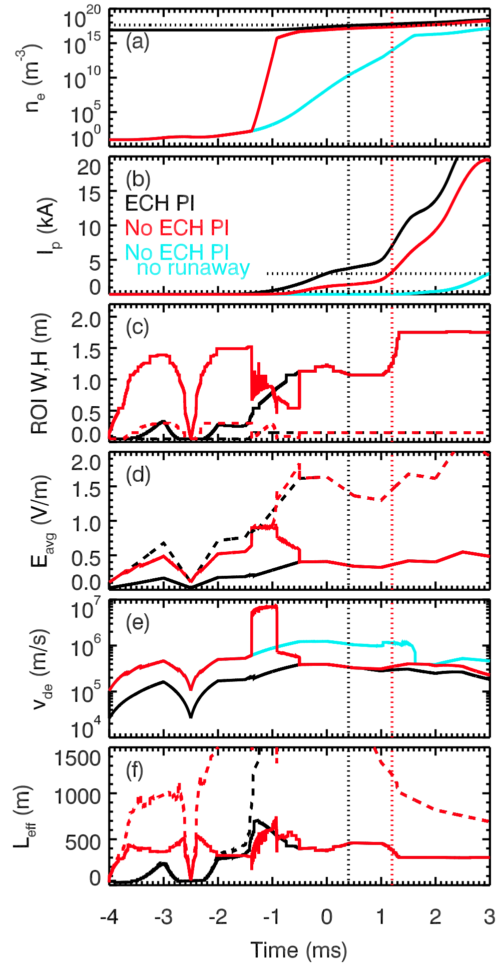


**Figure 6.** Reduced model of discharge breakdown derived from time-dependent vacuum calculations. The three colors use the same vacuum field evolution with different assumptions: large starting plasma density (black), and small starting plasma density allowing for runaway electrons (red) or using a constant drift velocity (blue).

collisions. The model includes an ad hoc factor to reduce the electron drift velocity once the density is above this threshold. The model does not include the modification of the field structure by the plasma poloidal magnetic field which is expected to play a role in improving confinement soon after initiation. Figure 6(*b*) shows the estimated plasma current where the horizontal dotted line at $I_p = 3$ kA corresponds to about 15 Gauss on the inboard Mirnov signal. The vertical black and red dashed lines correspond to the Initiation times (transition between PI and CR phases) shown in figure 5(*e*) for the discharge with (black) and without (red) ECH PI and the reduced model is in good agreement with this timing.

Figure 6(*c*) shows the ROI full width (dashed) and full height (solid) that maximizes equation (9) at each time point for the black and red calculations. The ROI is often a rectangle where the full height (solid) is greater than the full width (dashed). After $t = 0$, the width is about 15 cm, while the height is 100–180 cm. The size and elongated shape of the ROIs is consistent with the earliest detectable visible emission from the plasma made by fast camera imaging. The optimal ROI is different before $t = 0$ for the two cases due to the impact of the self-generated fields at large density. The field null enters the vacuum region around $t = +0.5$ ms, and the ROI rapidly increases in height due to a reduction of the poloidal curvature of the field (i.e. the field null has less radial curvature on the inboard side compared to the outboard side). This is a robust feature of the reduced model and produces a faster increase in $I_p$ once $B_Z$ changes direction. It is presumed that if the poloidal field produced by the plasma was self-consistently included in the calculation it would lead to a further reduction in the poloidal curvature and result in a taller ROI.

Figure 6(*d*) shows the average parallel electric field in each optimum ROI. The dashed lines are the average applied parallel electric field derived from the vacuum field calculations. The solid lines are the inferred $E_\parallel$ by subtracting an estimate of the self-generated cancellation (equation (8)) with the assumption that $E_{self}/E_\parallel \leqslant 75\%$. As seen by the comparison between the dashed and solid lines, $E_{self}$ significantly limits $E_\parallel$ once the density is greater than $10^{16}$ m$^{-3}$.

The average parallel drift velocity is shown in figure 6(*e*). The applied $E$ field becomes large enough around $t = -1.5$ ms to produce an $E$ field equal to the runaway threshold condition in the low-density case (red trace), producing a rapid increase in the electron velocity and rate of density rise. The rapid increase in the density continues until $E_{self}$ begins to limit $E_\parallel$ near $t = -1$ ms. In the black case, the large initial density means $E_{self}$ is a significant fraction of the applied field for the entire breakdown period, suppressing any entry into the runaway regime.

The bottom panel of figure 6 shows the calculation of the effective connection length where the solid line is $L_{avg}$ (equation (10*c*)) and the dashed line is the $L_{CZ}$ component (equation (10*a*)). The dashed lines are often much greater than the solid line, indicating that $L_{CR}$ is the component restricting the effective connection length between 400–500 m. The effective connection length is much larger for wider ROIs, however the maximum increase in $I_p$ is optimized in elongated (H $\gg$ W) ROIs due to the strong 1/R fall-off of the $E$ and $B_T$ field in STs.

One robust result from the model is that the short delay (~1 ms) in the initiation time between cases with (black) and without PI is only reproduced if the model assumes the electrons can 'run away' (red case) independent of the choice of the free parameters. Using a model without the runaway condition (blue), produces a larger delay (~3 ms). The results from the experiment and reduced model demonstrate that ECH PI has little impact on the evolution of the startup when operating with a prefill near 40 $\mu$Torr, good timing of the field null (a few ms after the start of $V_{loop}$) and low impurity content.

A unique DI discharge on NSTX was produced by reducing the solenoid precharge from 24 to 12 kA without changing the feed-forward programming of the poloidal field coils (127655) delaying the field null until $t = +9$ ms when $V_{loop}$ is nearly constant. Figure 7(a) shows the measured inboard $B_Z$ while the other panels show the plasma density, $I_p$, $E_{avg}$, $v_{de}$ and $L_{avg}$ computed with the reduced model using the same assumptions in the three cases as described with figure 6. This discharge achieves a larger $L_{eff}$ compared to the discharges in figure 6 since halving the solenoid precharge reduces the poloidal field curvature and increases the height of the field null region. The

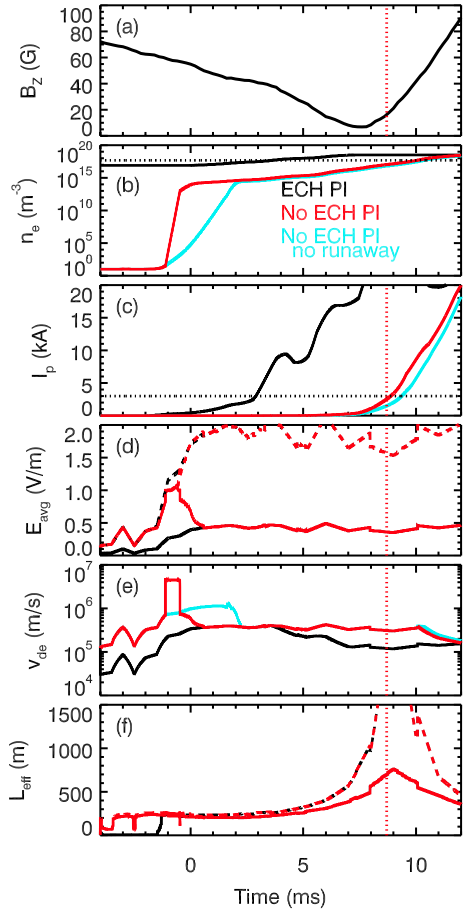


**Figure 7.** (*a*) $B_Z$ measured at inboard midplane for a discharge with a delayed field null. Reduced model calculations for (*b*) electron density, (*c*) plasma current, (*d*) applied $E$ field (dashed) and plasma $E$ field (solid), (*e*) electron drift velocity and (*f*) effective connection length (solid) and $L_{CZ}$ component (dashed).

discharge did not use ECH PI and no comparison discharge was taken that did use ECH PI. The delay between the start of the applied voltage at $t = -1$ ms and the initiation time (vertical dotted red line) is only reproduced when using the assumption of a large self-induced $E$ field. The model predicts that without ECH PI (red case) the runaway regime is still accessed prior to $t = 0$, however the density rises slowly once $E_{\text{self}}$ begins to limit the $E$ field. This transition occurs at lower density compared to the cases in figure 6 due to the larger pitch angle of the vacuum field. The agreement between the reduced model and this unique discharge constrains the choice of the maximum $E_{\text{self}}/E_{\text{applied}}$ ratio to be on the order of 75%. The model results suggest that ECH PI should have enabled the discharge to be initiated when $B_Z$ ~ 40 Gauss, demonstrating that the impact of ECH PI is more significant when attempting to initiate a discharge without a good field null.

The initiation of discharges with ECH PI at large (~40 Gauss) $B_Z$ fields is demonstrated in a set of discharges taken on NSTX-U shown in figure 8. The difference between the three discharges is the current in the equilibrium field coils (PF3) is altered to move the timing of the field null earlier (current in the coil is decreases 0.4 kA from black to red).

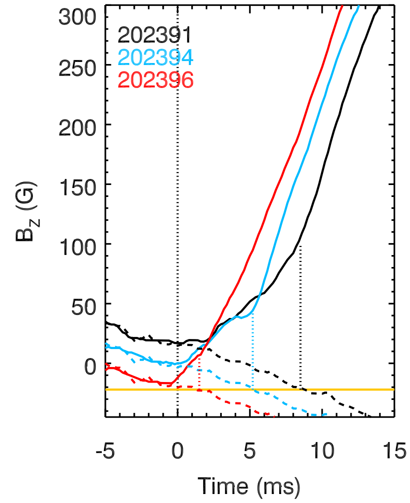


**Figure 8.** Measured inboard $B_Z$ from three NSTX-U discharges with ECH PI where the offset current of the PF3 coils is reduced to move the null timing earlier from black to red. Dashed lines are for a vacuum discharge matching the black case and scaled for the other two discharges. Orange and dotted lines highlight a correlation between the vacuum field being sufficiently negative and an inflection in the $I_p$ ramp rate.

The three solid lines are for discharges with a plasma, while the black dashed trace is for a vacuum discharge (202387) where the coil current programming matches 202391 (solid black). The blue and red dashed lines were created by shifting the black dashed line downward to provide an estimate of the vacuum field strength for the two additional plasma discharges. All three discharges produce a detectable plasma field near $t = +1$ ms despite a difference of ~40 Gauss in the vertical field strength when using ECH PI.

Later in this section, a model for the timescale of the CR phase (3 kA $< I_p <$ 20 kA) will be presented and compared to data. The discharges in figure 8 illustrate that one factor impacting the timescale is the direction of the vertical field after initiation. The intersection of the dashed (vacuum) lines with the orange horizontal line roughly correlate in time with an inflection in the rate $B_Z$ and $I_p$ increase as shown by the dotted vertical lines. The increase in the $I_p$ ramp rate with negative $B_Z$ is consistent with the reduction in the field curvature as discussed with figure 6. Furthermore, the negative $B_Z$ provides an appropriate equilibrium field for the current channel, facilitating an increase in the confinement of the electrons. The discharges in figure 8 demonstrate that ECH PI can initiate discharges prior to forming a field null, but the rapid rise in $I_p$ is delayed until after the vacuum vertical field is in the confining direction.

The significant result demonstrated in figures 6 and 7 is that the reduced model presented in equations (1)–(10) can reproduce the timescale of the PI phase for discharges with and without ECH PI across a range of observed initiation times. This agreement requires the assumption that the effective connection length is shorter than the parallel connection length computed using field-line following, a period of rapid ionization can occur with electrons in the runaway regime and that self-generated electric fields reduce the applied $E$ field above a critical density by up to 75%.

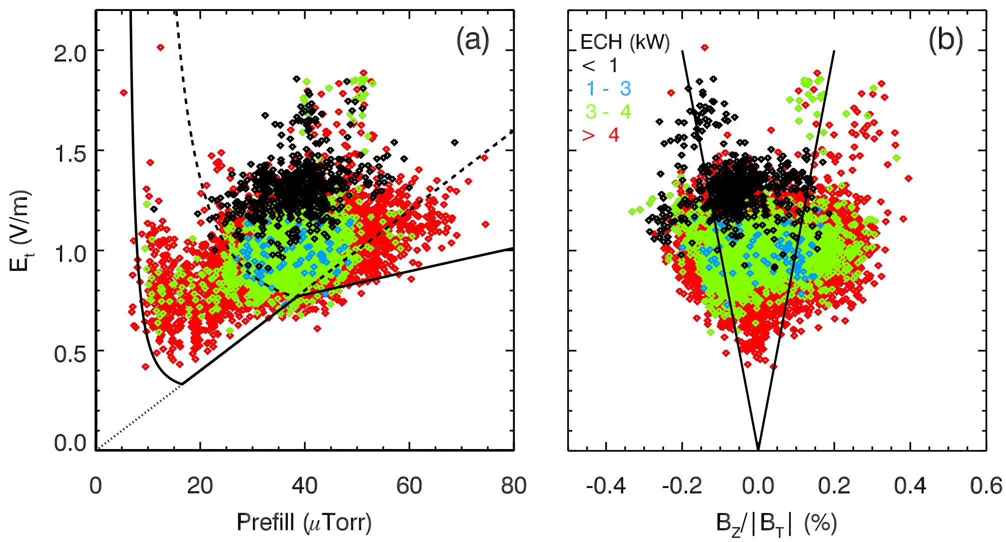


**Figure 9.** NSTX and NSTX-U DI database for 1 ms prior to first detectable $B_Z$ plasma signal. $E$ field at $R = 0.22$ m is plotted against ($a$) prefill and ($b$) ratio of inboard $B_Z$ and $B_T$ at $R = 0.22$ m. Points are colored by level of ECH PI.

*4.1.3. Comparison PI model with a large database.* A database of about 12 500 NSTX discharges and 250 NSTX-U discharges was created to provide an additional test for the reduced model and provide further insight on the impact of ECH PI. Most detailed studies of DI startup employ a relatively static field and $V_{loop}$ in order to form a database to best quantify the requirements and timescales for breakdown [20, 25]. The breakdown phase on NSTX employs a rapidly changing $V_{loop}$ and connection length, making the definition of the average $E$ and $B$ fields in the database sensitive to the choice of time ranges. Nevertheless, the phenomenology of the breakdown phase is found to be consistent with more controlled breakdown studies and the elements of the reduced model discussed with figures 6 and 7.

For all of the database plots, the $E$ and $B_T$ are computed at 5 cm outside the inner wall limiter (IWL) using the measured $V_{loop}$ and $I_{TF}$, respectively. Figure 9 shows the $E$ field averaged over 1 ms prior to minimum of the measured $B_Z$ plotted against the prefill (figure 9($a$)) and the ratio of the measured $B_Z/B_T$ (figure 9($b$)). Most discharges target a prefill in the range of 20–70 $\mu$Torr. The colors of the data points indicate the average ECH PI power with black being small ECH power (<1 kW) and red having the most heating power (4–30 kW).

The significant result from figure 9($a$) is that all of the discharges initiated without ECH PI (black points) occur in the runaway regime as designated with the diagonal line at $E/P = 20$ kV m$^{-1}$ Torr$^{-1}$. ECH PI (blue, green and red points) can initiate a discharge prior to achieving the runaway conditions, especially at larger prefill. Similarly, figure 9($b$) shows discharges with ECH PI can produce detectable fields prior to the appearance of the field null when $B_Z/B_T > 0$, especially when the ECH exceeds 3 kW (green and red). The solid lines in figure 9($b$) bound $E_T B_T/B_\theta > 1$ kV m$^{-1}$, which is a traditional criterion for reliable breakdown without PI (assuming $B_Z \sim B_\theta$) [20].

The contours in figure 9($a$) show the solution for equation (4) assuming $L = 400$ m, $t_{bd} = 1$ ms and $v_{De}$ is defined by equation (7) (runaway regime) above the dotted diagonal line and equation (5) below. The dashed contour shows $n_{ef}/n_{e0} = 10^{18}$ (per 1 ms) bounds most of the discharges without ECH PI consistent with the expectation that the runaway regime enables the rapid increase in density. The solid contour in figure 9a shows the minimum $E$ field required for $n_{ef}/n_{e0} = 10^3$ that bounds most of the data with significant ECH (red points).

The lowest $E$ field with modest ECH power (blue points with power < 3 kW) is achieved when the prefill is in the range of 35–45 $\mu$Torr. One possible reason is that most discharges targeted a 40 $\mu$Torr prefill, increasing the probability of a discharge achieving the fortuitous conditions (null timing, low impurity content) that produce the lowest $E$ field requirement. However, there may exist an optimal prefill pressure for the efficacy of the ECH, as reported in past studies [26]. This optimal prefill range aligns with the optimal prefill for discharges without ECH (black points).

ECH PI powers up to 30 kW have been used on NSTX, however the $E$ field required to initiate the discharge does not improve significantly for heating power above 4 kW. This is consistent with previous studies of ECH PI, where there is an abrupt transition in the achievable plasma density at a critical ECH power level (order several kW), and a smaller impact on the plasma density above this power level [20, 26]. It is proposed that the density saturation occurs when rapid drift losses of the high-energy electrons increase with ECH power and offset any improvement in the ionization rate.

The lower bound (both in $E$ and $P$) of the dataset indicates the maximum effective connection length ($L$) must be at least 400 m, enabling the breakdown to be successful down to 10 $\mu$Torr prefill. Only a small number of discharges (~10) failed to have a successful initiation in the decade of running NSTX. All of these discharges have a concurrent failure of the gas injection system (prefill < 15 $\mu$Torr) and the ECH PI system, consistent with the large increase in the required $E$ field that occurs with prefill < 10 $\mu$Torr.

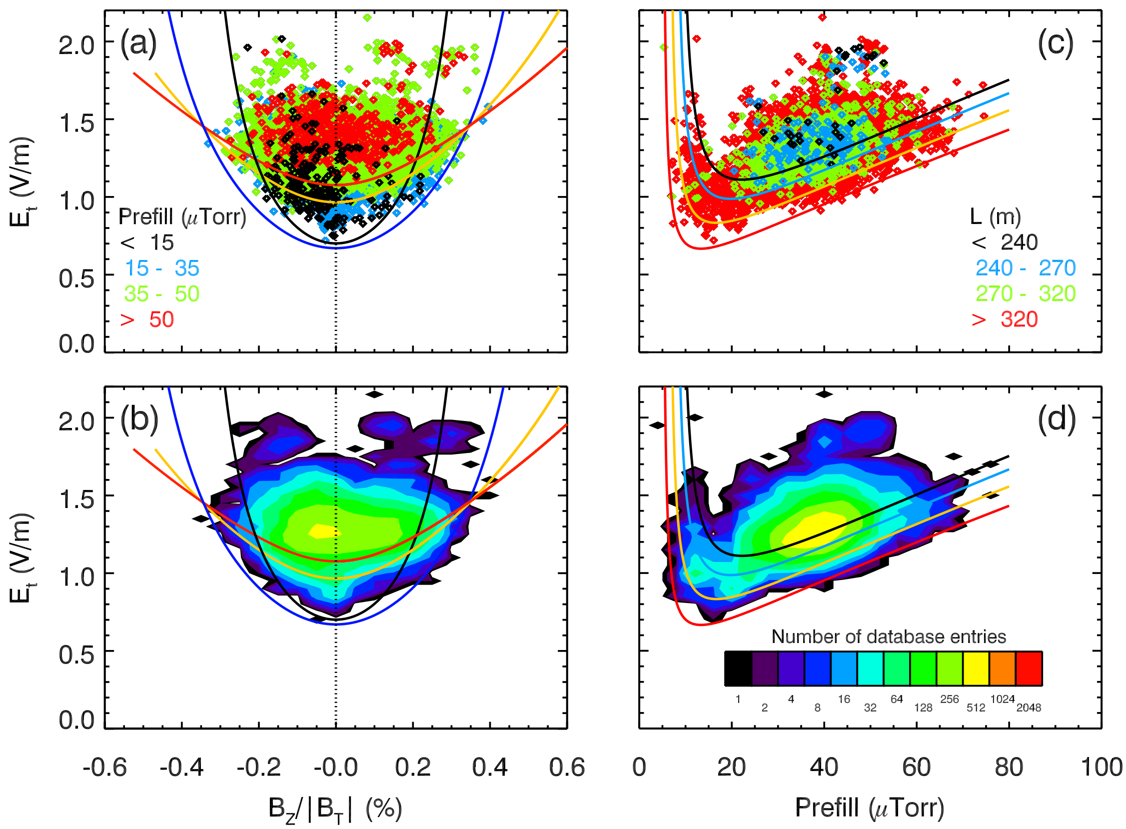


**Figure 10.** DI scenario database 1 ms prior to achieving 15 Gauss on the $B_Z$ measurement. Applied $E$ field at $R = 0.22$ m plotted against the (*a*) and (*b*) measured $B_Z/B_T$ and (*c*) and (*d*) the prefill. (*a*) and (*c*) show individual database points while (*b*) and (*d*) show the density of database entries. Solid lines show solution to $4 \times E_{min}$.

Two subsets of discharges from NSTX are omitted from the database presented in figure 9 but provide useful insight into the impact of pre-ionization. The first subset has an unintended breakdown during the solenoid precharge with reverse current and positive $B_Z$ about 30–100 ms prior to the desired start of the discharge. Although the null condition was avoided with finite $B_Z$, the connection length was large enough to support a breakdown. The reverse breakdown is undesirable because it leads to uncontrolled conditions at the desired startup time and the loss of the pre-breakdown plasma can liberate impurities from the wall. Nevertheless, the second breakdown initiates rapidly at low prefill (<20 $\mu$Torr) regardless of the level of ECH PI indicating that some residual plasma density remained after the loss of the pre-breakdown plasma. The second excluded subset have small (<0.5 $V_{loop}$) 50–100 Hz oscillations in the ohmic solenoid current prior to the breakdown phase due to issues with regulation of the solenoid current. The $V_{loop}$ oscillations do not produce detectable plasma signals or noticeably reduce the vessel pressure but are observed to reduce the critical $E_t$ for discharges without ECH PI. The technique of using oscillations in $V_{loop}$ as a pre-ionization technique has been demonstrated previously [11] and is useful in devices without dedicated PI systems.

The data in figure 9 examine the conditions prior to the earliest detection of plasma current. However, the viability of the startup requires a transition into the CR phase, which is found to correlate with the discharge reaching $I_p > 3$ kA. Figures 10 and 11 investigates the average $E$ field 1 ms prior to generating 15 Gauss above the minimum value on the inboard $B_Z$ measurement. The $E$ field is compared to the ratio of $B_Z/B_T$ in figures 10(*a*) and (*b*) similar to figure 9(*b*). As discussed with figure 5, the uncertainty in $B_Z/B_T$ is approximately 0.1%. The top panel (figure 10(*a*)) has a datapoint for each database entry where the colors indicate the prefill range. The bottom panel (figure 10(*b*)) shows contours indicating the density of data points, where each new color indicates a factor-of-two increase. The color bar included in figure 10(*d*) describes the contour shading in figures 10(*b*) and (*d*) and figures 11(*b*) and (*b*). The data follows the convention described in section 2, where negative $B_Z$ is in the confining direction. The highest density of discharges is initiated near the time when $B_Z = 0$ corresponding to the timing of the field null.

The solid lines in figure 10 are derived from the requirement that the ionization rate must exceed the loss rate in order to sustain the avalanche. This leads to a minimum $E$ field

$$E_{min}\left(\mathrm{V\,m^{-1}}\right) > \frac{1.25 \times 10^4\, P\,(\mathrm{Torr})}{\ln\left(510\, P\,(\mathrm{Torr})\, L\,(\mathrm{m})\right)} \qquad (11)$$

where the lines plot $4 \times E_{min}$. The requirement that the applied $E$ field is four times larger than $E_{min}$ is consistent with the reduced model where the self-generated $E$ field reduces the applied field by 75% at the densities required to enter the

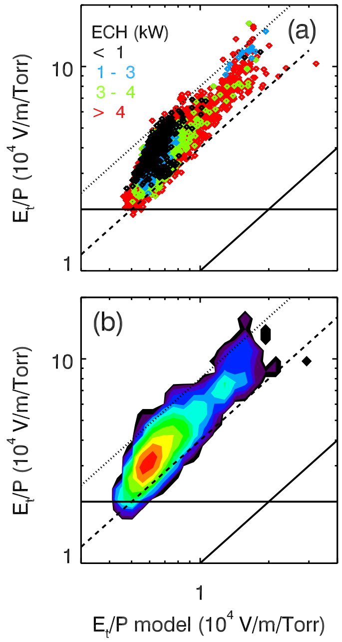


**Figure 11.** Comparison of the database to equation (11).

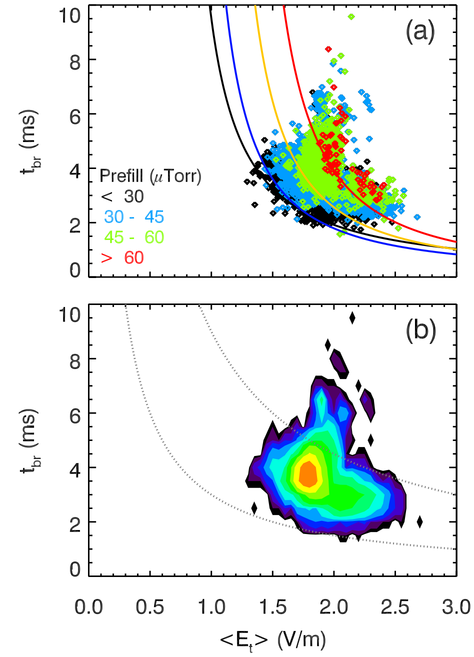


**Figure 12.** Timescale of increasing from 15 to 115 Gauss plotted versus time-averaged *E* field. (*a*) Database points colored by prefill with solid lines corresponding to equation (15). (*b*) Density of database entries with dotted lines indicating contours of ohmic flux consumption.

CR phase. Thus, while the self-field may oppose only a small fraction of the applied *E* field initially (figure 9), it is a large fraction of the applied field once $I_p \sim 3$ kA.

The black, blue, orange and red solid lines in figures 10(*a*) and (*b*) show the solution for $4 \times E_{min}$ using a prefill (*P*) of 10, 15, 35 and 50 $\mu$Torr, respectively. The *x*-axis is related to the effective connection length by simplifying equation (10):

$$L_{eff} = \left[\left(\frac{2}{H_{ROI}}\frac{B_{Z,mirnov}}{B_T}\right)^2 + \left(\frac{1}{400\,\text{m}}\right)^2\right]^{-1/2}. \quad (12)$$

The modifications to equation (10) are motivated by the calculations in figure 6 where $L_{CR}$ is nearly constant at 400 m. Figure 10(*a*) shows that $H_{ROI} = 1.8$ m produces contours of $4 \times E_{min}$ that are in agreement with the predicted trends with the prefill and connection length. This implied ROI height is larger than the prediction from the reduced model (figure 6(*c*)), most likely due to the error in measuring $B_Z$; reducing $H_{ROI}$ reduces the width of the U-shaped contours.

Figures 10(*c*) and (*d*) show the average *E* field versus the discharge prefill. Figure 10(*c*) is similar to figure 9(*b*), except that the datapoints are now colored by the approximate effective connection length using equation (12). The black, blue, orange and red solid lines in figures 10(*c*) and (*d*) show the solution for the $4 \times E_{min}$ field using $L = 240$, 270, 320 and 400 m, respectively. The contours mostly bound the colored datapoints, indicating that initiating a discharge at lower prefill and lower *E* field requires a larger *L*. Figure 10(*d*) shows contours indicating the density of database entries, where each new color indicates a factor-of-two increase.

Figure 11 summarizes the comparison of the *E/P* computed 1 ms prior to achieving 15 Gauss with the minimum *E/P* field derived from equations (11) and (12). The solid diagonal line is unity, where the experimental *E/P* matches $E_{min}/P$. The solid black horizontal line indicates the approximate transition to the runaway regime (20 kV m$^{-1}$ Torr$^{-1}$). The dashed diagonal line indicates where the experimental *E/P* is a factor of four larger than $E_{min}/P$ consistent with $E_{self}$ being 75% of the applied electric field. The dotted diagonal line indicates $8 \times E_{min}/P$ where the discharges approaching this level occur in experiments with larger impurity content.

*4.1.4. Model for timescale of the CR phase.* The reduced model calculations shown in figure 6 illustrate that, for typical prefill levels, the plasma density becomes large enough in the CR phase such that the electron velocity slows down due to the increasing collision frequency with ions. The electron drift velocity depends on the effective resistivity of the partially ionized plasma from electron collisions with neutrals and ions. The electron drift velocity with dominant electron-ion collisions including neoclassical plasma resistivity is

$$v_{De} = \frac{E}{\eta_{nc} n e} = 1.9\left[\frac{\text{m}^2\,\text{Torr}}{\text{V s eV}^{3/2}}\right]\frac{T_e^{\frac{3}{2}}\left(1-(r/R)^{1/2}\right)^2}{Z\ln\Lambda(n_e/n_N)}\frac{E}{P} \quad (13)$$

where $n_e/n_N$ is the ratio of the plasma density to the initial neutral density where $n_N(\text{m}^{-3}) = 6.4 \times 10^{22}\ P(\text{Torr})$. The drift velocity from equation (13) (electron–ion collisions) is slower than equation (5) (electron–neutral collisions) when $n_e/n_N = 14\%$ and assuming Spitzer resistivity ($r/R \sim 0$), a pure hydrogenic plasma ($Z = 1$), the Coulomb logarithm ($\ln\,\Lambda$) is on the order of 10 and $T_e = 10$ eV, as reported in previous studies [20]. Combining equations (4) and (13) and assuming $\ln\Lambda = 10$, $n_{e0} + n_{ef} \sim n_{ef}$ and $T_e = 10$ eV, the length of the CR phase is

$$t_{\mathrm{br}} = \frac{Z\ (n_{\mathrm{ef}}/n_{\mathrm{N}})\ \ln(n_{\mathrm{ef}}/n_{\mathrm{e0}})}{\left(1-(r/R)^{1/2}\right)^2}\left(0.083\left(\mathrm{V\,s\,m^{-1}}\right)\right)\ \frac{P}{E\,(\alpha-1/L)}. \quad (14)$$

Figure 12(*a*) shows the time required to increase from 15 to 115 Gauss above the minimum inboard $B_Z$ versus the average $E$ field during this period. This period represents the CR phase ($I_p$ increasing from about 3 to 20 kA) that ends near the timing of the $D_\alpha$ peak when $n_{ef}/n_N$ ~ 0.5 and takes about $4 \pm 2$ ms for most discharges on NSTX and NSTX-U. The datapoints are colored by prefill and the electric field required to achieve the shortest breakdown periods increases with prefill. The solid lines show $t_{br}$ derived from equation (14) using

$$t_{\mathrm{br}}(\mathrm{ms}) > 1.7\frac{83}{E_{\mathrm{eff}}}\frac{P}{(AP\exp(-BP/E_{\mathrm{eff}})\ -1/L_{\mathrm{eff}})} \quad (15)$$

where the $E_{eff}$ is 25% of the time-averaged applied $E$ field (V m$^{-1}$) during the period required to increase the measured $B_Z$ from 15 to 115 Gauss and $L_{eff} = 400$ m. The colored lines show calculations using $P = 10$, 30, 45 and 60 $\mu$Torr, respectively. The best agreement, particularly with the variation with prefill, is obtained by reducing the applied $E$ field by a factor of four rather than altering the leading coefficient or altering $L_{eff}$.

The leading coefficient of equation (15) is consistent with reasonable estimates for the leading term of equation (14). For example, assuming $Z = 1$, $n_{ef}/n_N = 0.5$ and Spitzer resistivity ($r/R$ ~ 0) implies $n_{ef}/n_{e0} > 30$ or that the plasma density increases from 1.6 to 50% of the starting neutral density during the CR phase. Increasing the plasma resistivity due to impurities ($Z > 1$) or neoclassical enhancement ($r/R > 0$) implies $n_{ef}/n_{e0}$ is smaller for the same breakdown time. It is noted that NSTX-U and MAST-U will produce discharges at larger aspect ratio than NSTX, and thus the neoclassical enhancement of the classical resistivity is predicted to be smaller, leading to a predicted reduction in $t_{br}$ compared to NSTX. The limited data from NSTX-U was not included in figure 12 but was generally consistent with the NSTX database; more data, particularly direct measurements of the density and $Z_{eff}$, is needed for a definitive investigation.

The important result from figure 12 is that the timescale of CR phase is longer than assuming the drift velocity is set solely by the electron-neutral collisions (equation(5)) and consistent with Spitzer resistivity provided $E_{eff}$ is 25% of the applied $E$ field. The 75% reduction in the $E$ field and $L_{eff} = 400$ m match the assumptions that describe the fastest PI phase evolution. This implies that the dominant loss mechanisms do not change significantly as the plasma generated poloidal field begins to form closed magnetic surfaces. One possibility is that magnetic stochasticity allows open field lines to penetrate the closed magnetic surfaces. Furthermore, there are processes that slow the evolution of the CR phase, such as the plasma inductance and neutral screening and recycling, that are not captured in these equations.

The largest impact of impurities in the breakdown phase is the timescale of the plasma current increase and the timing of the $D_\alpha$ peak. The discharges that initiate at 6–8 $\times$ $E_{min}$ (figure 11) and with $t_{br} > 6$ ms (figure 12) all come from conditions expected to have large impurity content (for example, during campaigns to condition the RF antenna). Almost all discharges that failed on NSTX come from this subset where the plasma resistance was larger and $I_p$ did not increase fast enough to be consistent with the increasing vertical magnetic field in the burn-through phase. Furthermore, operation at large prefill (red points in figure 12) with this DI scenario had a small operational window for achieving $t_{br} < 6$ ms and were more likely to fail with $E_T$ below 2.0 V m$^{-1}$.

The plasma current at the end of the breakdown phase (~20 kA) derived from magnetic measurements is consistent with a reasonable estimate of the plasma geometry ($R$ ~ 0.3 m, $S$ ~ 0.5 m$^2$, $V$ ~ 1 m$^3$), density (10$^{18}$ m$^{-3}$) and electron drift velocity (10$^5$ m s$^{-1}$). The total volume of NSTX is ~25 m$^3$, thus the plasma occupies only a small fraction of the vacuum volume. The total number of electrons in the plasma ($N_e$ ~ 10$^{18}$) is on the order of 10% of the remaining neutral inventory within the NSTX volume at the time of the $D_\alpha$ peak. This implies that the $D_\alpha$ peak corresponds to the approximate time when the local density of electrons and neutrals are equalized within a region surrounding the plasma, but not the equalization of the total inventory of electrons and neutrals within the vacuum vessel. The observation that $I_p$ ~ 20 kA at the $D_\alpha$ peak is specific to the DI scenario and geometry on NSTX and NSTX-U and may require reevaluation for other scenarios or geometries.

The ECH PI system is often injecting during the entire breakdown phase, but the database indicates that the details of the ECH injection have little impact on the timescale of the CR phase. The insensitivity to ECH during the CR phase is consistent with power balance estimates where several kW of heating power has little impact on the achievable $T_e$. Discharges without ECH PI tend to initiate at larger $E$ and consequently have a shorter CR phase. Thus, the small delay in the initiation resulting from the absence of ECH PI was often partially compensated by a shorter CR phase resulting in a negligible difference in the timing of the $D_\alpha$ peak when operating with a prefill around 40 $\mu$Torr.

The reduced model defines the length of the CR phase ($t_{br}$) using equation (15) and defining $E_{eff} = E_{avg}/4$ where $E_{avg}$ is the average of the $E$ field required to be in the runaway regime ($E = 0.02\ P(\mu\mathrm{Torr})$) and the lower limit of the $E$ field at the start of the burn-through phase described in the next section. This $E_{avg}$, combined with the assumption that $L_{eff} = 400$ m, produces a conservative estimate for the time required to increase $I_p$ from 3 kA to 20 kA in the predictive calculations (section 6).

## 5. Equilibrium and stability metrics for the burn-through phase

The beginning of the burn-through phase (20 kA $< I_p <$ 200 kA) is accomplished using feed-forward control of the ohmic solenoid and poloidal field coil current to provide the $V_{loop}$ and equilibrium vertical field required for a target d$I_p$/d$t$. At sufficiently large $I_p$ ($I_p$ ~ 200 kA), the magnetic field generated

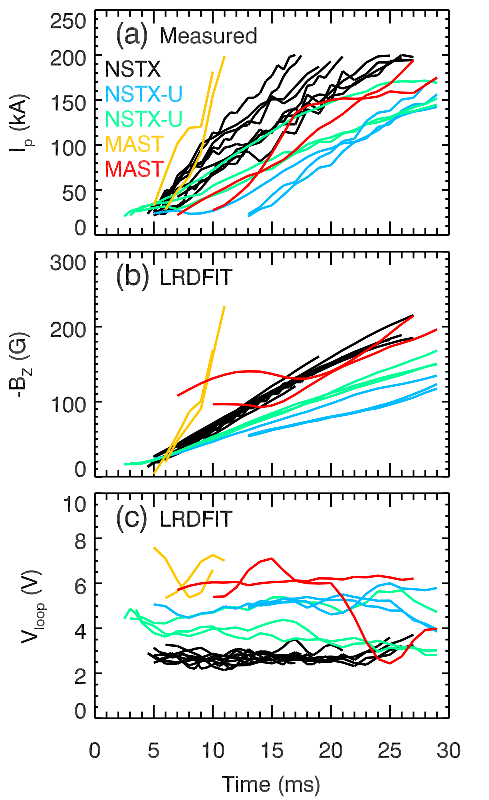


**Figure 13.** DI startup discharges from NSTX (black), NSTX-U (blue and green) and MAST (orange and red). (*a*) Measured plasma current and computed (*b*) $-B_Z$ and (c) $V_{\mathrm{loop}}$ in the vacuum region.

by the plasma dominates uncompensated pickup from the vacuum field and control of the solenoid and poloidal field coil current transitions to real-time feedback on the measured $I_\mathrm{p}$ and the vertical and radial position of the plasma current centroid.

The goal of this section is to use successful startup discharges to develop reasonable targets for the plasma equilibrium and stability during the $I_\mathrm{p}$ ramp up. One consideration is the definition of a region of interest (ROI) where the vacuum fields ($B_Z$, $B_\mathrm{R}$ and $V_{\mathrm{loop}}$) are evaluated in lieu of a rigorous equilibrium and stability calculation. For the purposes of a simplified analysis using vacuum field calculations, it is assumed the discharge shape has triangularity near unity (i.e. a 'D' shape) and the current distribution is force-free (i.e. zero-beta). The force-free equilibrium has $J \propto B \sim B_\mathrm{T}$, thus at low aspect ratio with a 'D' shape, the current is concentrated as a vertical sheet near the IWL and the current centroid is close to the IWL. The choice of the time and space averaging of the vacuum fields has a minimal impact on the general conclusions of this work provided a consistent definition is used in both the derivation of the empirical constraints and the predictive calculations. The ROI used for the following analysis is a rectangle with a total height of 1.0 m and a width of 0.15 m similar to the hashed region in figure 3, reflecting that most of the current is assumed to be near the IWL. Note that this is a ROI of fixed dimensions, whereas the ROI in the breakdown model (section 4) has a size that can change in time.

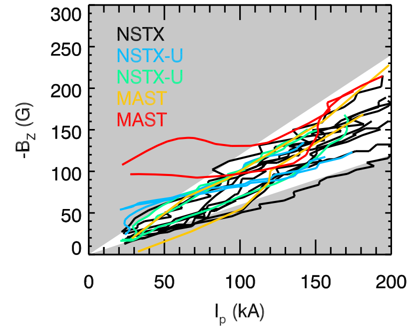


**Figure 14.** $-B_Z$ versus $I_\mathrm{p}$ for the traces shown in figure 13.

Figure 13 shows the measured plasma current and the average vacuum $B_Z$, and $V_{\mathrm{loop}}$ in the ROI computed using LRDFIT for select discharges on NSTX (black), NSTX-U (blue and green) and MAST (orange and red) with) versus time for times prior to 30 ms when 20 kA < $I_\mathrm{p}$ < 200 kA. The standard NSTX startup scenario (black) did not change much over the course of ten years of operation, thus, the evolution of $B_Z$ and $V_{\mathrm{loop}}$ are similar for all discharges considered. MAST explored a variety of startup scenarios with different $I_\mathrm{p}$ ramp rates. Two examples (17418 and 19563) use a capacitor bank on the P3 coils to get a fast rise in $-B_Z$ after 9 ms (orange). Two other MAST examples (12283 and 19716) do not use a capacitor bank (red) and are restricted to a slower rise in $-B_Z$. NSTX-U favored slower $I_\mathrm{p}$ ramp rates compared to NSTX due to constraints from vertical stability, which are discussed later. Three discharges with an 8 kA solenoid precharge (green) have a steady ramp in $I_\mathrm{p}$, while the three discharges using the 20 kA precharge have a delay in the increase in $I_\mathrm{p}$ (blue) due to an unoptimized scenario with a mismatch between a longer breakdown time and the $B_Z$ evolution.

The data shown in figure 13 are used to derive semi-empirical targets for the evolution of the vacuum fields in order to achieve self-consistent radial force balance, inductive current drive and passive vertical stability in the early portion of the burn-through phase. These targets constrain predictive calculations for NSTX-U and MAST-U and provide quantifiable metrics for evaluating DI scenarios.

### *5.1. Radial force balance*

Figure 14 shows the vacuum $B_Z$ versus $I_\mathrm{p}$ for the same discharges and time periods in figure 13. The shaded regions bound $0.6 < -B_Z/I_\mathrm{P}$ (G kA$^{-1}$) < 1.2, where most discharges follow

$$-B_Z/I_\mathrm{P}\left(\mathrm{G\,kA^{-1}}\right) = 0.9 \tag{16}$$

particularly when $I_\mathrm{p} > 100$ kA. Fast visible camera images for the two MAST discharges with large $-B_Z/I_\mathrm{p}$ early in the discharge (red) indicate the discharge shape has a small radial width until $I_\mathrm{p} > 100$ kA. Conversely, discharges near the lower range of $-B_Z/I_\mathrm{p}$ lead to plasma shapes with large radial extent. The equilibrium $B_Z$ is expected to have a weak dependence on the major radius of the plasma using the assumptions of the shape and current distribution described earlier, especially if it

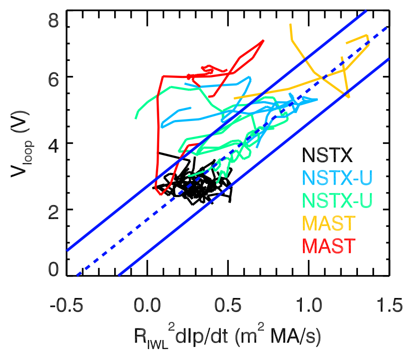


**Figure 15.** $V_{loop}$ versus $I_p$ ramp rate multiplied by $R_{IWL}{}^2$. Dark blue lines are linear offset fit (dashed) with ±1 V offset (solid).

is assumed the elongation of the plasma boundary decreases as the aspect ratio increases. This is consistent with the observed invariance in the $B_Z/I_p$ ratio between the devices with different radii of the inner wall limiter ($R_{IWL}$).

### 5.2. Inductive current drive

The feed-forward loop voltage must drive the desired $I_p$ ramp rate that is consistent with the evolution of $B_Z$. The circuit equation for a toroidal ohmic plasma is:

$$V_s = L_i \frac{dI_p}{dt} + \frac{1}{2} I_p \frac{dL_i}{dt} + V_r \quad (17)$$

where $V_s$ is the surface voltage and $V_r$ is the resistive voltage leading to ohmic heating of the plasma. The plasma inductance is typically approximated using:

$$L_i = \mu_0 \frac{R_0}{2} \ell_i \quad (18)$$

where $\ell_i$ is the internal inductance related to the distribution of the current within the plasma. Decent agreement can be found for the examples considered using reasonable assumptions for the time-dependent free parameters. However, a simpler model provides better agreement where the current is treated as a single turn solenoid with current equal to $I_p$ and the current is distributed at radius of the inner wall limiter ($R_{IWL}$) with a length of $h$ equal to the full height of the fixed ROI:

$$L_i = \mu_0 \frac{\pi R_{IWL}^2}{h}. \quad (19)$$

Assuming that the d$L$/d$t$ and $V_r$ terms are roughly constant over the startup period produces the relationship:

$$V_s = 3.9 \frac{R_{IWL}^2}{h} \frac{dI_p(\text{MA})}{dt} + V_r. \quad (20)$$

This is consistent with the empirically derived correction to the Ejima scaling proposed for low aspect ratio devices with an $R_0^2/a$ dependence [18]:

$$\Delta\psi_s \sim 0.4(R_0/a)\mu_0 I_p R_0. \quad (21)$$

Figure 15 shows the $V_{loop}$ from the vacuum field calculations versus $R_{IWL}^2 dI_p/dt$ where $dI_p/dt$ is from the experimental measurement. The dashed dark blue line in figure 15 solves equation (20) with $h = 1.0$ m and $V_r = 1.7$ V and the solid dark blue lines show ±1 V. One implication of this relationship is that the $V_{loop}$ required for a target $dI_p/dt$ increases rapidly with the radius of the breakdown region. The resistive voltage ($V_r$) is sensitive to factors that impact the plasma temperature, such as impurity content and neutral fueling rate. Discharges with enhanced impurities increase the $V_{loop}$ requirement for a target rate of increase in $I_p$. Consistent with equation (21), discharges that achieved small $-B_Z/I_p$ (larger radial width) tend to have a smaller $V_r$ while discharges with larger $-B_Z/I_p$ have a larger value. This is consistent with the expectation that the total surface area of the plasma interacting with the limiter increases as the radial width of the plasma decreases. Often this is simply described as 'pushing the plasma too hard into the limiter' and leads to enhanced impurity sputtering.

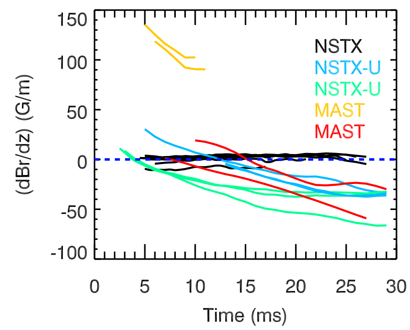


**Figure 16.** Average $dB_r/dZ$ at top and bottom segments of ROI. More negative values indicate the plasma is more at risk for becoming vertically unstable.

*5.2.1. Vertical stability.* The third consideration for the field evolution during ramp-up is that the plasma must remain vertically stable without active feedback (passive stability). A conservative estimate (ignoring image currents in conducting structures) is to enforce that the vacuum $B_R$ increase in strength as the plasma rigidly moves vertically away from the midplane. This equates to a positive $dB_r/dZ$ integrated along the ROI boundary:

$$\frac{1}{S} \oint \frac{dB_R}{dZ} \cdot \hat{R}\, dS > 0 \quad (22)$$

where $S$ is the length of the ROI boundary and $\hat{R}$ is a unit vector along $R$. This metric assumes the current density ($J$) has no $Z$ dependence and scales with $1/R$ such that $JRB_R \sim B_R$.

The metric derived from equation (22) is shown in figure 16 where a positive value indicates passive stability. Note that the magnitude of the stability metric is sensitive to the choice of the ROI whereas the other metrics discussed in this section are less sensitive. Figure 16 illustrates that discharges do remain stable with a negative value for the choice of the ROI in this analysis; however, the experience from NSTX-U is that these discharges operated near the margin for passive stability. Current induced in the copper cooling tubes on NSTX-U limited the achievable elongation and the $I_p$ ramp rate early in the ramp up by degrading the field curvature relative to NSTX. The smaller $dI_p/dt$ compared to NSTX was pursued to lower the $V_{loop}$ requirements in order to achieve passive stability for

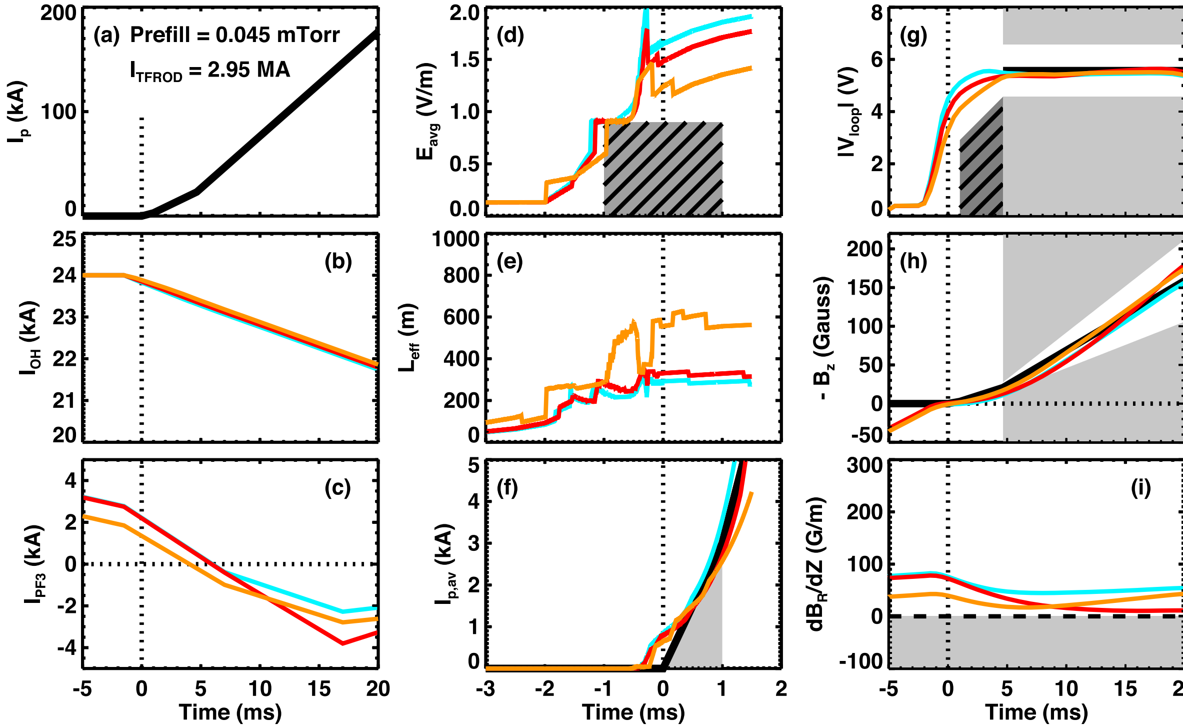


**Figure 17.** Predictive calculations for DI scenarios on NSTX-U. First column summarizes free parameters including the target (*a*) $I_p$, (*b*) solenoid current and (*c*) PF coil current. Second column summarizes breakdown model (section 4) and the third column summarizes the equilibrium and stability targets (section 5). Red traces use the conducting structures from the 2016 operation. Blue traces switch the cooling tube material from copper to Inconel. Orange traces modify the blue calculations by adding PF2 current to improve the field null at the expense of vertical stability.

a typical starting plasma shape. The MAST scenarios that used the P2 divertor coils to partially null the solenoid field (red) increase the vertical extent of the field null at the consequence of vertical stability early in the breakdown phase. This scenario was also observed to operate with marginal passive vertical stability.

Another common metric for vertical stability is the field index or decay index evaluated at the current centroid [27]. This expression assumes a dipole equilibrium field, and that the current is concentrated at the current centroid. Evaluating equation (22) at the boundary of an ROI was favored over the field index metric since the field structure at breakdown tends to be multi-pole, the current is close to the boundary (low inductance) and the magnitude of $B$ is small in the early ramp-up phase, leading to large variations in the field index across the stability threshold.

## 6. DI scenario calculations for MAST-U and NSTX-U

The semi-empirical reduced model (figure 1) derived in sections 4 and 5 are used to guide and constrain the development of DI scenarios for MAST-U and NSTX-U. The constraints for the predictive calculations require four scalar input parameters: (1) the target initiation time, (2) the target $\mathrm{d}I_p/\mathrm{d}t$ following the breakdown phase, (3) the prefill, and (4) the TF rod current. The feedforward solenoid and poloidal field coil current waveforms are modified by the user in LRDFIT to develop scenarios that satisfy the breakdown metrics, technical constraints and the desired pre-charge strategy.

The primary goal of the NSTX-U calculations is to examine the potential to increase the $I_p$ ramp rate to aid in the development of low-$\ell_i$ discharges. This process informs the design of the ongoing modifications of NSTX-U, particularly by quantifying the impact of changes to the conductive wall elements. The primary goal of the MAST-U calculations is to provide guidance for developing options for DI startup during the first operational campaign.

The DI scenario developed during NSTX-U operations in 2016 had issues with vertical stability shortly after the startup phase when operating with $V_{loop} > 4.5$ V due to the large induced currents in the copper cooling tubes. Thus, a startup scenario with a slower $I_p$ ramp rate (~6 MA s$^{-1}$) compared to NSTX was developed to maintain $V_{loop} < 4.5$ V and achieve reliable startup. A rebalancing of the PF3 and PF5 currents to improve the vertical stability at larger ramp rates was not pursued to the fullest extent during operations.

Figure 17 summarizes LRDFIT calculations performed to develop DI scenarios for NSTX-U that achieve an $I_p$ ramp rate of 10 MA s$^{-1}$ after the breakdown phase, similar to what was realized on NSTX. The red traces summarize a scenario using the conducting structures from the 2016 campaign, while the light blue and orange traces are developed after switching the material of the cooling tubes from copper to Inconel in the simulation to capture changes in the redesign of NSTX-U.

All scenarios use a 45 $\mu$Torr prefill, a TF rod current equal to the maximum achieved in 2016 (corresponding to an on-axis $B_T = 0.63$ T), and a maximum solenoid precharge (24 kA), which is larger than the maximum achieved in 2016 (20 kA). The larger precharge reduces the vertical extent of the field null compared to what was previously achieved.

The first column of figures 17((*a*)–(*c*)) summarizes the free parameters of the calculation. Figure 17(*a*) shows the target $I_p$ evolution where $I_p$ increases from 0 to 3 kA over the first millisecond, then rises to 20 kA over the duration of the breakdown phase and finally increases at the target $dI_p/dt$. The length of the breakdown phase ($t_{br}$) required to achieve 20 kA is determined using equation (15) assuming a minimum $V_{loop}$ shown as the dark hashed region in figure 17(*g*). As described in section 4, the minimum $V_{loop}$ is computed by interpolating between the value required to access in the runaway regime in the PI phase and the lower range of the $V_{loop}$ required for the target $dI_p/dt$ in the burn-through phase (equation (20) $-1$ V).

The biggest challenge in the DI scenarios for NSTX-U is achieving good passive vertical stability. This motivates using only the PF3 coil in the DI scenarios to provide the nulling and equilibrium field in the first 20 ms of the discharge. Figure 17(*c*) shows the current in the PF3 coils chosen for each scenario. Without assistance from the large-*R* coil sets (PF4 or PF5), the voltage on the PF3 coils is approaching the 2 kV limit during the periods with the largest rate of change. The orange scenario uses current in the PF2 coil set (not shown) to increase the vertical extent of the null at the price of passive vertical stability. The PF2 coil current in the orange scenario is a steady 3 kA up until $t = 0$, then ramps to zero current at +5 ms while remaining under the 1 kV voltage limit.

The second column summarizes the reduced model described in section 4 where the rectangular ROI size is optimized at each time step to maximize the increase in the electron inventory. All of the calculations assume there is no ECH PI in order to produce a conservative calculation. Figure 17(*d*) shows the average applied toroidal *E* field in the ROI and the hashed region designates the requirement for operating in the runway regime. The self-generated *E* field opposing the applied *E* field is limited to be less than 75% of the total field, as described in section 4. $E_{self}/E_{avg}$ is at this maximum for most of the breakdown phase resulting in $E_{avg} - E_{self} < 0.5$ V. Figure 17(*e*) shows the effective connection length in the ROI, which is below 400 m when only using the PF3 coil due to the increased poloidal field curvature at the maximum solenoid current. The final panel in the center column (figure 17(*f*)) shows the plasma current derived from the reduced breakdown model. The goal is to develop scenarios that achieve approximately 3 kA of plasma current at $t = +1$ ms. The orange calculation required the smallest $V_{loop}$ to achieve this target, while the light blue case required the largest. This is directly related to the height of the field null (i.e. the poloidal curvature of the field).

The final column of figure 17 summarizes the constraints on the burn-through equilibrium and stability described in section 5. In all cases, the same ROI shape used to develop the semi-empirical constraints in section 5 (a rectangle 1.0 m tall, 0.15 m wide). The loop voltage (figure 17(*g*)) must evolve to facilitate breakdown in the large *E/P* regime and increase $I_p$ during the breakdown and burn-through phases. The flattop $V_{loop}$ target (solid back line) is derived using equation (20) with $h = 1.0$ and $V_r = 1.7$ and the white region identifies $\pm 1$ V around the target, similar to figure 15. The target evolution of the vertical magnetic field (figure 17(*h*)) is derived using equation (16) and the white region indicates $\pm 0.3$ G kA$^{-1}$ similar to figure 14. As mentioned with figure 17(*c*), the PF3 voltage is approaching the 2 kV maximum in order to achieve the target $B_Z$ evolution with a 10 MA s$^{-1}$ $I_p$ ramp rate.

The final panel of the third column (figure 17(*i*)) shows the average $dB_R/dZ$ along the top and bottom horizontal segments of the ROI as described by equation (22) where a more positive value improves the likelihood of passive vertical stability. The poloidal field has significant curvature at breakdown at the largest solenoid precharge level, leading to good passive stability. However, the induced current in the polar regions degrades the good curvature later in the startup phase. The calculations suggest that despite using only the PF3 coils to provide the equilibrium field, the target passive vertical stability is marginal when targeting a 10 MA s$^{-1}$ $I_p$ ramp rate with the copper cooling tubes (red scenario). However, the modification of the cooling tube material when NSTX-U operations resume should allow the passive vertical stability constraint to be satisfied with ample margin (light blue). The fix to the cooling tubes will also reduce the demands on the PF3 current to provide adequate equilibrium field after $t = 8$ ms (figure 17(*c*)), however the reduction in the current induced in the polar regions increases the poloidal curvature of the field and reduces the maximum achievable connection length (light blue trace is slightly lower than the red trace in figure 17(*e*)) increasing the $V_{loop}$ requirement (figure 17(*d*)). Switching the cooling tube material to Inconel provides headroom on the passive stability, thus the addition of PF2 current is an option (orange traces) to increase the vertical extent of the field null and reduce the required $V_{loop}$. This may be important in scenarios that increase the critical $L_{eff}$ by operating at lower TF rod current.

The calculations presented in figure 17 suggest that the changes to the conductor structures during the rebuild of the NSTX-U polar regions and a re-optimization of the feed-forward coil currents should enable a DI scenario capable of $dI_p/dt = 10$ MA s$^{-1}$. Additional calculations using the Inconel cooling tubes found that the passive vertical stability limit becomes marginal for $I_p$ ramp rates around 13 MA s$^{-1}$ due to currents induced in the PF1A mandrels within the polar regions; these structures will not exist in the NSTX-U redesign and should allow further margin in the vertical stability at larger $I_p$ ramp rates. $I_p$ ramp rates exceeding 15 MA s$^{-1}$ require adding PF5 current after breakdown which degrades the passive vertical stability. Therefore, on NSTX-U, the voltage available to the PF3 coils and the passive vertical stability ultimately limit the maximum $I_p$ ramp rate provided the larger ramp rates are not limited by MHD stability.

Similar time-dependent vacuum calculations have been completed for MAST-U to assist the development of DI scenarios for the first operational campaign. Figure 18 summarizes two calculations using a prefill of 45 $\mu$Torr, an $I_p$ ramp

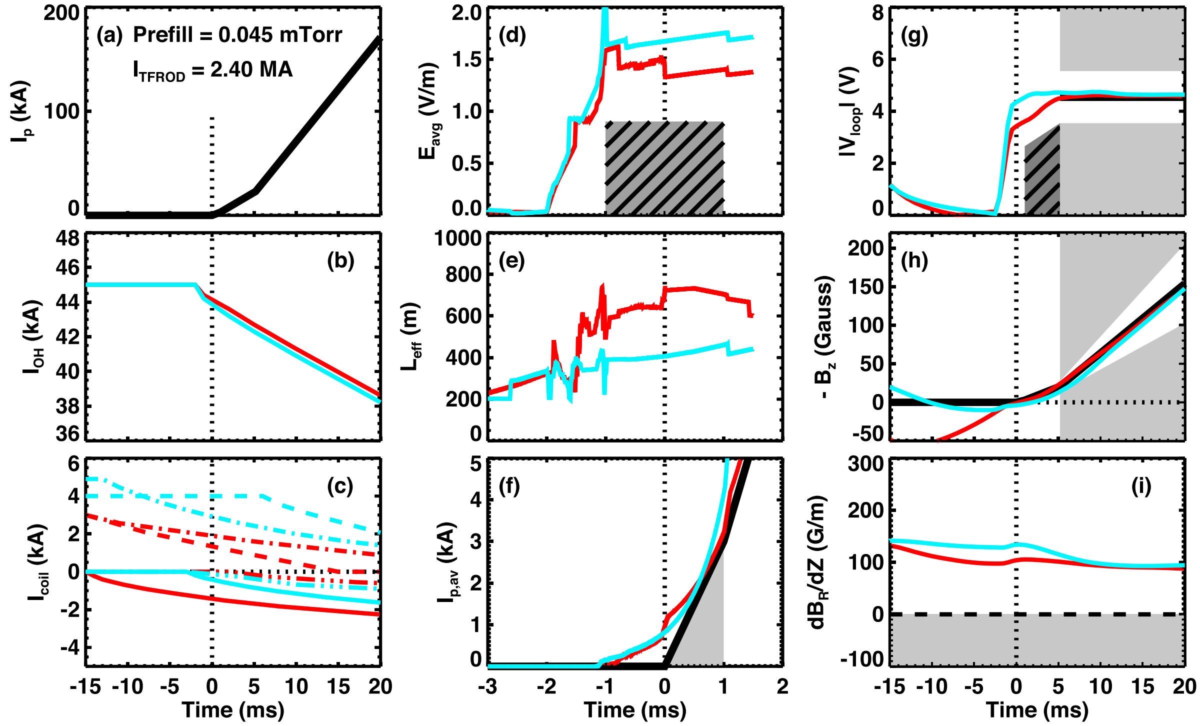


**Figure 18.** Predictive DI scenario calculations for the first operational campaign of MAST-U, similar to the calculations shown in figure 17. Red traces use six D-coil sets while the blue traces use three D-coil sets.

rate of 10 MA $s^{-1}$ and the maximum TF rod current permitted in the first campaign (2.4 MA). The red case uses six D coils (D1, D2, D3, DP, D6, D7) in addition to the P4 and P5 coil sets. All of the metrics are satisfied with the PF coils operated with sufficient margin from the current, voltage, heating and force limits imposed for the first campaign. The precharge aims to balance the $I^2t$ heating of the D-coils and minimize the heating of the solenoid coil (the dwell time of the solenoid at maximum current is 16.5 ms). The red case avoids a zero crossing of $B_Z$ during the gas injection period (starting at −15 ms). The current request for the D1, D2 and D3 is a constant 4 kA in the time range shown in figure 18 (not shown in plot). Figure 18(*c*) shows current in various coil sets including D6 and D7 (dash dot) and DP (dash) that achieve a maximum precharge current of +3 kA, and the negative current in P4 (solid) and P5 (dash with three dots).

The calculations demonstrate that MAST-U can achieve a DI scenario with ample margin to optimize the scenario during the first campaign. The lower induced currents in the polar regions on MAST-U allow for the low-*R* divertor coils to produce a high order field null (figure 18(*e*)) and still achieve good field curvature for passive stability (figure 18(*i*)). The calculations indicate the MAST-U scenarios with six D-coils will have head room to explore the trade-offs in improving the vertical extent of the field null at the expense of passive vertical stability. In separate calculations, the maximum $I_p$ ramp rate achieved using the maximum voltage on all of the PF coils is about 15 MA $s^{-1}$ with acceptable passive stability provided the larger ramp rates are not limited by MHD stability. Therefore, the maximum $I_p$ ramp rate on MAST-U is limited by the available voltage on the poloidal field coils. The behavior of the power systems when operating multiple sets at large voltage will be explored during the first power commissioning of MAST-U.

The viable MAST-U scenario (red traces) was extended to quantify the impact of technical, logistical or scenario considerations that may limit the use of a coil set. The light blue case in figure 18 examines the impact of limiting the startup scenario to three D-coil sets. This would most likely occur due to technical issues but could be used to minimize the heating of a particular coil set needed for long pulse discharges. The combination of D1, DP and D7 were found to provide the most plausible DI scenario when operating with the maximum solenoid precharge (45 kA) allowed in the first campaign. All of the D-coils operate at their current limits (D1 carries a constant 5 kA, not shown in (*c*)) and the DP (dashed), D7 (dash dot) and P4 (solid) power supplies operate at their respective voltage limits in order to get a suitable flux swing for an $I_p$ ramp rate of 10 MA $s^{-1}$. One challenge with this scenario is that it is difficult to exclude the field null prior to the desired breakdown time (figure 18(*h*)), which makes the scenario more at risk for an unconfined breakdown prior to $t = -2$ ms. Another challenge is that the scenario has limited margin for optimization since many of the coils are at the voltage and current limits. Thus, operating at the largest solenoid precharge and/or with an $I_p$ ramp rate of 10 MA $s^{-1}$ may be difficult if constrained to using only three D-coil sets. Similar calculations have been completed using this framework to develop scenarios at reduced solenoid precharge and using fewer than three D-coil sets; these may be attractive options for producing the 'first plasma' on MAST-U due to the simplicity of using fewer coil sets.

## 7. Discussion and conclusions

Direct induction (DI) startup is a long-standing technique for initiating discharges in tokamaks. Most tokamak devices develop one or more DI scenarios that reliably initiate a plasma discharge over a variety of experimental and technical conditions. This paper describes recent efforts to characterize the demonstrated DI scenarios on the world's largest spherical tokamak (ST) experiments and produce reduced models using time-dependent vacuum field calculations aimed at accelerating the development of reliable DI startup scenarios on the forthcoming NSTX-U and MAST-U devices. Both devices aim to achieve a reliable DI scenario that minimizes the flux consumption and maximizes the rise in plasma current ($I_p$) in order to and enable long-pulse discharges with low internal inductance.

The analysis and calculations described in this paper are a product of a recent focus at PPPL and CCFE toward developing shared tools and analysis to foster efficient collaboration between the ST experiments. The LRDFIT vacuum field calculations, combined with the semi-empirical models, will assist machine operators at both devices in interpreting and optimizing the performance of DI scenarios to achieve the experimental missions. The described framework aims to provide a 'control-room' tool where predictive calculations or analysis is completed within a minute or less.

The DI scenario developed on NSTX was reliable over a decade of operations. Only a handful of discharges on NSTX failed to achieve breakdown ($I_p$ ~ 20 kA) when both the gas injection and ECH PI systems did not operate correctly. The most common failure during the burn-through phase ($I_p > 20$ kA) was a 'fizzle' where the plasma current would not rise fast enough to be consistent with the equilibrium field provided by the feed-forward poloidal field coils due to large fueling or plasma impurity content. In preparation for NSTX-U operations in 2016, LRDFIT calculations were used to design a DI scenario that mimicked the NSTX scenario [10].

The effort to develop a reduced model with semi-empirical constraints (sections 4 and 5) using time-dependent vacuum field calculations was motivated by the desire to have a common framework for evaluating DI scenarios on different devices and to develop scenarios that may deviate from the standard NSTX scenario. This activity benefits from establishing a computationally efficient framework with conservative criteria for breakdown, equilibrium and stability. The detailed analysis of the DI startup on STs also supports the ongoing effort for improving models and understanding of the physics of DI startup when designing scenarios for ITER and future tokamak reactors.

Given a prescribed evolution of the ohmic solenoid current, it is trivial to use nulling field coils to produce a poloidal magnetic field singularity at a specific location and time in an axisymmetric calculation. At the outset of this work, it was unclear how to define the critical properties of the field null (such as the spatial boundaries of the low-field region or the length of time it must exist) required to evaluate the likelihood of a successful discharge initiation. The model described in section 4 was developed such that the boundary of a rectangular region-of-interest (ROI) is chosen at each time step of the vacuum field calculation to maximize the increase in the plasma current (equation (9)) and the time-integration of the electron production (equation (2)) is computed in order to estimate the plasma density and current evolution. The loss rate of the electrons ($1/L_{\mathrm{eff}}$) is computed by separately calculating the radial and vertical components of the free-streaming loss rate over the ROI (equation (10)). In agreement with experimental observations, the ROI near the Initiation time is a tall rectangle near the inner wall limiter where the dominant loss rate is due to radial transport of the electrons. Thus, the loss rate is mostly impacted by the vertical extent of the field null ($\mathrm{d}B_R/\mathrm{d}Z$) with little influence from the radial extent of the null ($\mathrm{d}B_Z/\mathrm{d}R$). The $L_{\mathrm{eff}}$ (~400 m) for the NSTX scenario derived from this technique is in good agreement with a large database of DI startup for NSTX and NSTX-U. Although NSTX achieved large field nulls that should support connection lengths on the order of 2000 m, the reduced model identifies that the critical parameter is reducing the radial magnetic field in the region close to the inner wall limiter.

One significant observation made when comparing existing theory to the experimental data is that STs readily access the runaway avalanche regime where the bulk of electrons are freely accelerating over the open magnetic field lines when operating without pre-ionization. This regime is facilitated on STs since electric fields on the order of 1 V m$^{-1}$ are produced in the low-$R$ breakdown region at modest loop voltage (2–4 V). This was demonstrated in the detailed analysis of a single DI scenario on NSTX (figures 5 and 6) where the runaway regime is accessed about 1.5 ms prior to the initiation time. Further evidence was provided in figure 9 where all discharges without ECH PI (black points) occur above the critical $E$ field for entering the runaway regime. This work provides an explanation for why ECH PI on NSTX had little impact on the startup evolution with a prefill around 40 $\mu$Torr.

As shown in the database analysis of NSTX and NSTX-U discharges, ECH PI allows for discharges to initiate at a lower $E$ field than what is required for the runaway regime. The interpretation presented in figures 6 and 7 is that ECH PI produces a plasma density in the range of $10^{14}$–$10^{17}$ m$^{-3}$ and thus only a small increase in the density is needed to produce detectable magnetic fields. This small increase can occur within 1 ms even when the electrons achieve a slower, constant drift velocity. Another possible interpretation is that the ECH produces a population of high-energy electrons that reduce the $E$ field required to produce a significant population of runaway electrons capable of driving a rapid initiation. More diagnostic measurements and modelling are needed to identify the important mechanisms of ECH PI.

The evolution of the initial rise in $I_p$ (from zero to 20 kA) is reproduced in the reduced model when assuming that poloidal charge separation limits the parallel electric field driving the electron motion (equation (8)). This assumption is motivated by recent high-fidelity modeling of the breakdown process that achieved impressive agreement with experimental measurements on KSTAR. More investigation is needed if the level of cancellation (75%) that provided a good match to NSTX data is consistent with the self-generated $E$ field from charge separation, whether this effect can persist as the plasma magnetic field begins to form closed magnetic surfaces and how this effect may scale to different scenarios or devices. Furthermore, breakdown on STs would benefit from similar high-fidelity calculations performed at large $E$ fields to investigate the feasibility of the runaway electron model.

Once the plasma density is on the order of 15% of the local neutral density, the electrons begin to collide more frequently with ions and the electron drift speed is reduced, slowing the evolution of the plasma density. The timescale of initial current increase (figure 12) was consistent with the assumptions of Spitzer resistivity, although more data on the plasma properties (temperature, density, impurity content) are needed for a definitive comparison. The conditions for initiating the discharge and timescale for increasing the $I_p$ up until the $D_\alpha$ peak are similar (75% reduction of the $E$ field and $L_{eff} = 400$ m). The expectation was the formation of closed magnetic surfaces would result in a smaller $E_{self}$ and/or larger $L_{eff}$; more investigation is needed to quantify the requirements for forming closed magnetic surfaces and the phenomenon driving the reduction in $E$ field and the loss rate during the breakdown phase.

Section 5 examines the evolution of representative discharges from NSTX, NSTX-U and MAST-U to develop semi-empirical targets for the feed-forward evolution of the magnetic and electric fields that maintain good equilibrium and stability in the early burn-through phase. One unique observation is that the equilibrium field (figure 14) and plasma inductance (figure 15) is reproduced when assuming most of the current is in a long, thin sheet near the centre column and thus, can be treated as a single-turn solenoid. This current distribution is consistent with the assumption of force-free current where $J \propto B \propto R^{-1}$ and that the plasma cross-section is an elongated 'D' shape.

A critical component of the DI scenario is that the discharge achieves passive vertical stability. This requirement limited the operational space for DI startup on NSTX-U due to large induced currents in the polar regions of the device. A metric for stability was developed in section 5 based on an assumed vertical extent of the plasma and demonstrated that the NSTX-U DI scenarios operated with marginal vertical stability. The vertical stability calculation is sensitive to the choice of the plasma ROI and would benefit from coupling the vacuum field calculations to a free-boundary plasma equilibrium solver or a current filament model such that the equilibrium and stability of the plasma boundary can be directly evaluated.

Section 6 presents the application of the reduced model for predictive calculations for NSTX-U and MAST-U summarized in figures 17 and 18. Given a target $I_p$, prefill and TF rod current, the target current evolution of the ohmic solenoid and PF coils are manually adjusted to satisfy both the DI scenario metrics and the technical limits (coil current, voltage, forces and heating). The NSTX-U calculations aimed to investigate the impact of increasing the solenoid precharge current on the breakdown and reducing the induced currents in the polar regions. The calculations demonstrated that changing the cooling tube material from copper to Inconel should enable $I_p$ ramp rates of at least 10 MA $s^{-1}$ and could provide adequate head room on the vertical stability to include the PF2 coils in the scenario to improve the vertical extent of the field null at the largest values of solenoid current precharge. The MAST-U calculations demonstrate that the DI scenarios at the largest solenoid precharge require at least five poloidal field coil sets (P4, P5 and three D-coils) to achieve suitable breakdown and a 10 MA $s^{-1}$ ramp-up. Increasing the number of D-coil sets to six provides sufficient headroom for optimizing the balance between the vertical extent of the field null and the passive vertical stability. Two potential challenges in the MAST-U scenario are operating the poloidal field coil sets near the voltage limits to achieve 10 MA $s^{-1}$ and avoiding a field null during the reverse bias phase of the precharge when using only three D-coil sets. Both devices may be able to achieve $I_p$ ramp rates on the order of 15 MA $s^{-1}$, where the eventual limit is predicted to be the vertical stability on NSTX-U (subject to the final design of the polar region of the device) and the voltage on the PF coils on MAST-U (subject to conservative technical limits established for the first operational campaign). MHD instabilities from driving large edge current density can also limit the $I_p$ ramp rate, although the relatively large $B_T$ compared to $I_p$ tends to stabilize MHD instabilities in the early phase of the discharge.

The reduced models and metrics coupled to time-dependent vacuum field calculations presented in this paper provide an efficient framework for developing feed-forward DI scenarios and interpreting results on ST devices. Like any reduced model, additional data and high-fidelity modeling [7, 8] will aid in the refinement of the model. Operations on NSTX-U and MAST-U will potentially expand the database for testing and refining the semi-empirical models, particularly at larger $V_{loop}$ as the major radius and target $I_p$ ramp rate increases. The work presented in this paper may also motivate more controlled investigations of the breakdown on STs where the $E$ field and null quality are scanned independently while maintaining the other properties nearly static. Continued DI startup experiments and analysis on smaller ST experiments would provide a valuable test for the semi-empirical models.

## Acknowledgments

The authors thank the NSTX and MAST teams that developed the DI scenarios used in this analysis. This work was supported by the US DOE under Contract DE-AC02-09CH11466. This work has been part funded by the RCUK Energy Programme (Grant No. EP/P012450/1). The digital data for this paper can be found at http://arks.princeton.edu/ark:/88435/dsp01cv43p067x.

## ORCID iDs

D.J. Battaglia https://orcid.org/0000-0001-8897-9740
J.E. Menard https://orcid.org/0000-0003-1292-3286

## References


[1] Mueller D. 2013 The physics of tokamak start-up *Phys. Plasmas* **20** 058101
[2] Menard J.E. *et al* 2012 Overview of the physics and engineering design of NSTX Upgrade *Nucl. Fusion* **52** 083015
[3] Morris W. *et al* 2018 MAST Upgrade divertor facility: a test bed for novel divertor solutions *IEEE Trans. Plasma Sci.* **46** 1217–26
[4] Gerhardt S.P., Andre R. and Menard J.E. 2012 Exploration of the equilibrium operating space for NSTX-Upgrade *Nucl. Fusion* **52** 083020
[5] Menard J. *et al* 2002 Ohmic flux consumption during initial operation of the NSTX spherical torus *Nucl. Fusion* **41** 1197–206
[6] Gates D. *et al* 2006 Progress towards steady state on NSTX *Nucl. Fusion* **46** S22–8
[7] Yoo M.-G. *et al* 2018 Evidence of a turbulent $E \times B$ mixing avalanche mechanism of gas breakdown in strongly magnetized systems *Nat. Commun.* **9** 3523
[8] Kim H.T., Fundamenski W. and Sips A.C.C. 2012 Enhancement of plasma burn-through simulation and validation in JET *Nucl. Fusion* **52** 103016
[9] Leuer J.A. *et al* 2017 Tokamak start-up modeling and design for EAST first plasma campaign *Fusion Sci. Technol.* **57** 48–65
[10] Battaglia D.J. *et al* 2018 Scenario development during commissioning operations on the National Spherical Torus Experiment Upgrade *Nucl. Fusion* **58** 046010
[11] Yamazaki H. *et al* 2018 Pre-ionization by AC Ohmic coil operation in the TST-2 spherical tokamak *Nucl. Fusion* **58** 016012
[12] Sips A.C.C. *et al* 2015 Progress in preparing scenarios for operation of the international thermonuclear experimental reactor *Phys. Plasmas* **22** 021804
[13] de Vries P.C. and Gribov Y. 2019 ITER breakdown and plasma initiation revisited *Nucl. Fusion* **59** 096043
[14] Berzak Hopkins L. *et al* 2012 Plasma equilibrium reconstructions in the lithium tokamak experiment *Nucl. Fusion* **52** 063025
[15] Menard J.E. *et al* 2006 Observation of instability-induced current redistribution in a spherical-torus plasma *Phys. Rev. Lett.* **97** 095002
[16] Appel L.C. *et al* 2006 A unified approach to equilibrium reconstruction *33rd EPS Conf. Plasma Physics (Rome, Italy, 19–23 June 2006)* P-2.184 (http://crpppc42.epfl.ch/Roma/pdf/P2_184.pdf)
[17] Gates D.A., Menard J.E. and Marsala R.J. 2004 Vessel eddy current measurement for the National Spherical Torus Experiment *Rev. Sci. Instrum.* **75** 5090–3
[18] Gryaznevich M., Shevchenko V. and Sykes A. 2006 Plasma formation in START and MAST spherical tokamaks *Nucl. Fusion* **46** S573–83
[19] Bigelow T.S., Peng M., Wilson J.R., Carter M.D. and Batchelor D.B. 1997 ECH on NSTX *AIP Conf. Proc.* **403** 211–4
[20] Lloyd B. *et al* 1991 Low voltage Ohmic and electron cyclotron heating assisted startup in DIII-D *Nucl. Fusion* **31** 2031–53
[21] Jiang W., Peng Y., Zhang Y. and Lapenta G. 2016 Numerical modeling of tokamak breakdown phase driven by pure Ohmic heating under ideal conditions *Nucl. Fusion* **56** 126017
[22] Peng Y. *et al* 2018 On the breakdown modes and parameter space of ohmic tokamak start-up *J. Plasma Phys.* **84** 905840505
[23] Hammond K.C., Raman R. and Volpe F.A. 2018 Application of Townsend avalanche theory to tokamak startup by coaxial helicity injection *Nucl. Fusion* **58** 016013
[24] Papoular R. 1976 The genesis of toroidal discharges *Nucl. Fusion* **16** 37–45
[25] de Vries P.C. *et al* 2013 Characterisation of plasma breakdown at JET with a carbon and ITER-like wall *Nucl. Fusion* **53** 053003
[26] Ocho T. *et al* 1980 Microwave preionization of the tokamak discharge at the electron cyclotron resonance *Phys. Lett.* A **77** 318–20
[27] Lazarus E.A., Lister J.B. and Neilson G.H. 1990 Control of the vertical instability in tokamaks control of the vertical instability in tokamaks *Nucl. Fusion* **30** 111